Ice Breakup Dates on 18 Eurasian Lakes Estimated by MODIS Data from 2001 to 2005

Takashi Nonaka (PASCO Corporation),
Tsuneo Matsunaga (National Institute for Environmental Studies),
Akira Hoyano (Tokyo Institute of Technology)

Background

・Snow and ice is widely taken up as one of the important indices showing climate change. "Ice breakup date of the lake and river has become early about fewer weeks over the past century." (IPCC, Intergovernmental Panel on Climate Change, 2001)

・However, few in-situ data of the ice breakup date exists on Eurasian continent. (For example, Lake Baikal)

・Remote sensing is especially useful to estimate the ice breakup dates for the lakes with no available in-situ data.

We developed the method to estimate the ice breakup dates in previous studies.

In this study, the ice breakup dates on 18 Eurasian lakes from 2001 to 2005 are estimated and the relationships between ice breakup dates and local climate will be discussed.

Relationships between ice breakup dates and local climate
(E.g., Lake Mendota, Lake Monona, WI, USA)

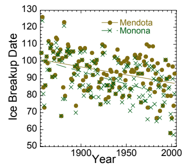

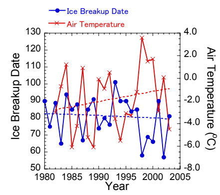

Ice breakup date has become early, and mean air temperature in spring has become an increase.

Ice Breakup Date:
first day when a specific area of lake surface is completely free of ice

Ice on the Rokannonmiike, at Miyazaki prefecture.

Method

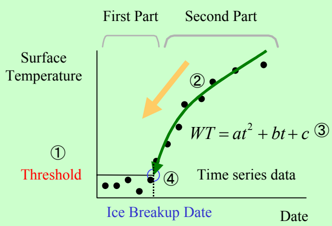

Breakup Temperature (Threshold) Estimation ①

Lake Surface Temperature Calculation ②

Water Temperature Trend Regression Equation ③

Intersection of Threshold and Equation ④

↓

Ice Breakup Date

Validation

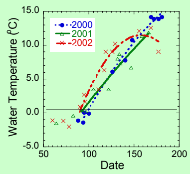

Saroma-ko Lagoon

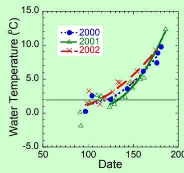

Lake Baikal

Saroma-ko Lagoon

	Estimation	Observation	Difference
2000	103	102	+1
2001	99	105	-6
2002	96	97	-1

Lake Baikal

	Estimation	Observation	Difference
2000	122	119	+3
2001	132	132	0
2002	117	118	-1

Accuracy is better than 3 days.

Usable satellite data

Requirement of satellite sensor for estimating ice breakup date
・observing everyday (short revisiting time)
・having near infrared band as well as thermal infrared band
→ MODIS AVHRR etc. is suitable

Data accuracy is very good, and various products are prepared.
→ MODIS is especially suitable

	MODIS	AVHRR	ASTER
Launch	1999	1978	1999
Band	32	5	14
Spatial resolution	1 km	1.1 km	90 m
Observation frequency	Everyday	Everyday	Every 16 days
Features	High Accuracy Various products		

Breakup Temperature

1 ℃ change of breakup temperature

↓

10 days changes of the ice breakup dates (for some lakes)

Accurate breakup temperature estimation is important.

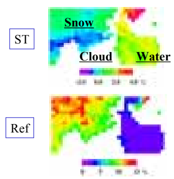

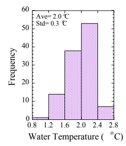

2.0 ℃ (freshwater)
0.5 ℃ (seawater)

Results

・Ice breakup dates of the center of each lake were estimated using MODIS Level 3 SST data.
・Breakup temperature of all lakes was set to 2.0 ℃ of freshwater.

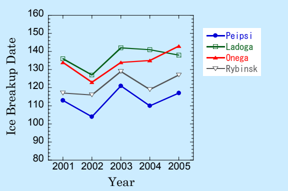

Area 1

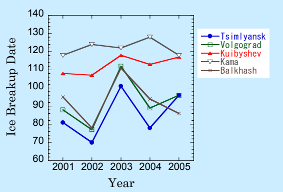

Area 2

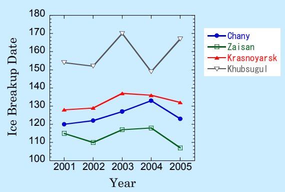

Area 3

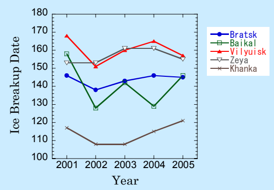

Area4

No	Lake	Latitude, Longitude	Elevati-on (m)
1	Peipsi	58.4 N, 27.4 E	30
2	Ladoga	60.5 N, 31.2 E	5
3	Onega	61.5 N, 35.2 E	35
4	Rybinsk	58.0 N, 38.5 E	102
5	Tsimlyansk	48.2 N, 43.1 E	36
6	Volgograd	50.2 N, 45.4 E	15
7	Kuibyshev	54.5 N, 49.4 E	53
8	Kama	58.3 N, 56.1 E	109
9	Balkhash	45.4 N, 76.2 E	341
10	Chany	54.5 N, 49.4 E	106
11	Zaisan	48.0 N, 83.5 E	341
12	Krasnoyarsk	54.5 N, 91.4 E	243
13	Khubusgol	51.0 N, 100.2 E	1645
14	Bratsk	54.4 N, 102.1 E	402
15	Baikal	53.4 N, 106.4 E	456
16	Vilyuisk	62.5 N, 111.1 E	244
17	Zeya	54.2 N, 128.1 E	315
18	Khanka	44.5 N, 132.2 E	69

・Ice breakup dates in 2002 and 2004 are relatively earlier for some of the lakes (especially area 1 and 2).
・Clear trend of the time series of the ice breakup date is not observed for lakes at high elevation (area 3) .
・Ice breakup dates in 2005 is earlier than in 2004 for some of the lakes in area 3 and 4.

↓

Time series of the ice breakup dates are related with the trend of mean air temperature ??

18 study lakes on the Eurasian continent.

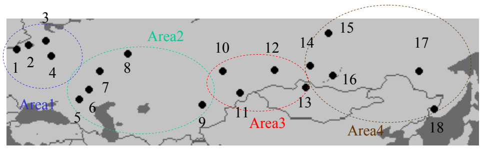

Relationships between ice breakup dates and local climate

・Ice breakup date data were estimated by the suggested method.
・Air temperature data at the center of each lake were derived from NCEP/NCAR data set, and averaged from March to May.

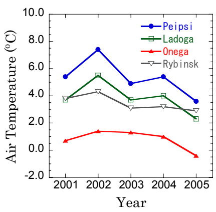

Mean air temperature in area 1

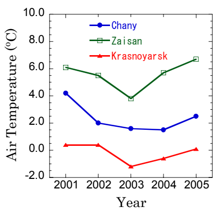

Mean air temperature in area 3

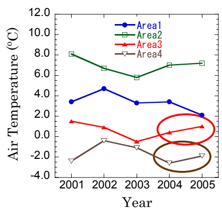

Mean air temperature for each area

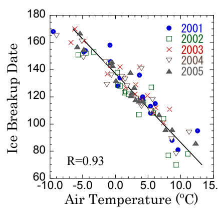

Ice breakup date and mean air temperature

・Annual changes of the ice breakup date are mostly can be explained from the mean air temperature.

・1 day change of the ice breakup date represents the 0.2 ℃ changes of the mean air temperature from March to May

Summary

Ice breakup dates on 18 Eurasian lakes from 2001 to 2005 were estimated using MODIS data.

The annual changes of the ice breakup date are different by the location, elevation, and local climate.

Ice breakup dates are strongly related with air temperature, and 1 day change represents 0.2 ℃ changes.

Future study

Long term of the ice breakup dates will be discussed, and the trend of the climate changes will be derived.

Effects of the 2004 Indian Ocean tsunami in Thailand based on ASTER images

Fumio YAMAZAKI[1], Ken'ichi KOUCHI[2], Masashi MATSUOKA[3]

[1] Professor, Department of Urban Environment Systems, Faculty of Engineering, Chiba University, Japan.

[2] Graduate Student, University of Tokyo, Japan. [3] Team Leader, EDM, NIED, Japan.

Introduction

High-resolution satellite (QuickBird, IKONOS) images were employed and GPS-synchronized photos/videos were taken in the damage survey after the 26 December 2004 Indian Ocean Tsunami in the south Thailand. Terra-ASTER images were also used to identify tsunami inundation areas comparing the pre-event and post-event images.

Tsunami Damage Survey in Thailand with GPS and Satellite Images

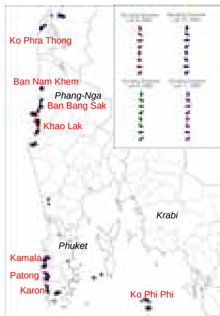

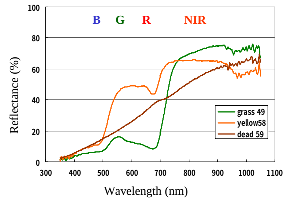

A reconnaissance survey was carried out by a team consisting of researchers from Thailand, Japan and USA. The objective of the survey is to gather geo-referenced tsunami inundation and damage information with the enhanced use of satellite images and GPS. Spectral reflectance of various surface materials were also obtained as ground truth data.

Tsunami Inundation Mapping Using ASTER Images and SRTM

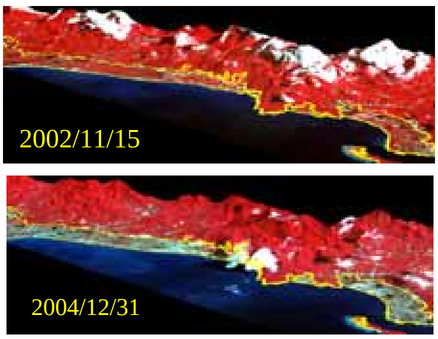

False color ASTER images of Khao Lak overlying on SRTM 90m DEM

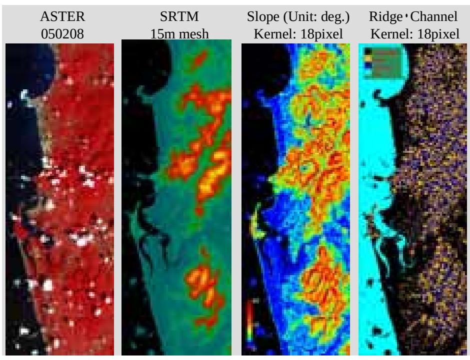

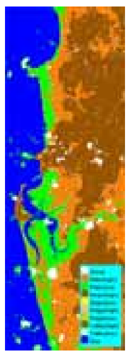

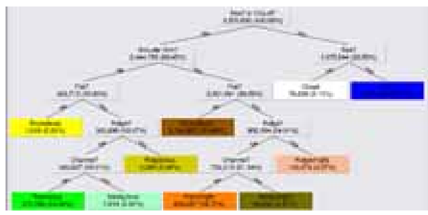

Decision tree of landform classification using ASTER images and SRTM 90m DEM

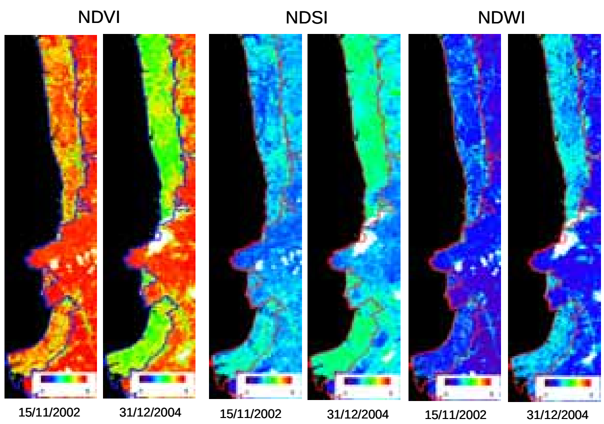

ASTER images were used to identify tsunami inundation areas using the changes in the normalized difference vegetation index (NDVI), soil index (NDSI), and water index (NDWI). It is found that tsunami caused the decrease of NDVI and the increase of NDSI and NDWI.

References

Yamazaki, F., Matsuoka, M., Warnitchai, P., Polngam, S., and Ghosh, S. (2005) Tsunami Reconnaissance Survey in Thailand Using Satellite Images and GPS, *Asian Journal of Geoinformatics*, Vol. 5, No. 2, pp. 53-61.

Kouchi, K., Yamazaki, F., Matsuoka, M., (2006) Tsunami Damage Detection Using Moderate-resolution Satellite Imagery, *Asian Conference on Earthquake Engineering*, Manila, Philippines.

The 11th CEReS International Symposium on Remote Sensing
"Maximization of the use of satellite data for understanding the earth environment"
13-14 December 2005, University Convention Hall (Keyaki Kaikan), Chiba University, Chiba, Japan

Vegetation and Water Analyses of Industrial Waste Using Remote Sensing

Hachinohe Institute of Technology

Wenhui Zhao, Takanori Sasaki and Shigetaka Fujita

Abstract

After an illegal dumping site was found on the border between Iwate and Aomori Prefectures, an environmental monitoring system using artificial satellites and ground observation apparatus was established to constantly monitor and analyze environmental changes. In this study, the data collected using this system, including satellite data, on-site, infrared camera images, and water quality data, was analyzed to establish the level of on-site contamination and state of recovery. Some SPOT images were compared to establish the on-site vegetation changes using the NDVI (Normalized Difference Vegetation Index). The relationship between changes in water quality and rainfall was established. It was confirmed that the removal of fluid waste and extensive work carried out on the site reduced the alkalinity of the water.

Key Words: Industrial waste, Remote sensing, Vegetation analysis, Water quality

Introduction

One of the biggest illegal dumping sites in Japan was found on the border between Iwate and Aomori Prefectures. Its area is 27 hectares, and the total amount of waste is about 820,000 m^3. It caused major social problems such as environmental contamination. An environmental monitoring system was established to collect and analyze the environmental data on-site. This system is very useful for establishing the level of contamination and state of recovery on and around the site.

Aerial photograph of illegal dumping site (April 25, 2005)

The satellite data such as multispectral SPOT image was analyzed for environmental analyses in the wide area, and the data from on-site sensors including water quality data and weather data was analyzed in detail.

The waste is taken away in trucks, but this will take several years to complete. In the meantime, the waste has been covered with tarpaulins to avoid pollution spreading before disposal. Waterproof walls will be set up around the site.

Environmental Monitoring System

Artificial satellites and ground observation apparatus were used in this environmental monitoring system. Data from NASA's Terra-1 and Aqua EOS satellites was received directly by an antenna installed on the roof of a building on our campus. Moreover, SPOT images, DEM data, and Quickbird images were analyzed by the ENVI software.

Five water quality analyzers, weather measuring equipment and two infrared cameras were set up at the dumping site. Data was then transmitted to the monitoring PC every three minutes. The items measured were pH, electric conductivity, flow rate, air temperature, and precipitation.

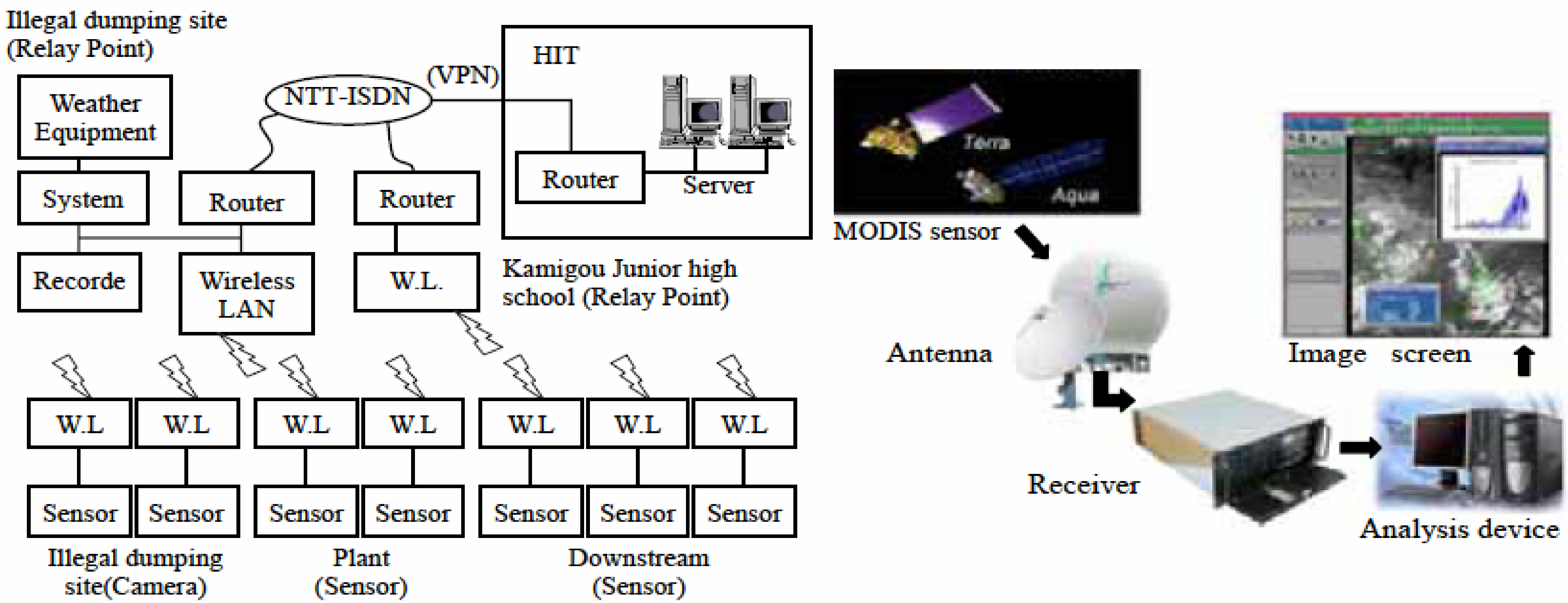

a. On-site observation system b. Reception and analysis system of satellite data

Vegetation Analysis using NDVI

The NDVI was used to transform multispectral data into a single image band representing vegetation distribution. The NDVI values indicate the amount of green vegetation present in the pixel — near-infrared radiation minus visible red radiation divided by near-infrared radiation plus visible red radiation. Written mathematically, the formula is: NDVI = (NIR - RED)/ (NIR + RED).

Very low NDVI values (0.1 and below) correspond to barren areas of rock, sand, or water. Moderate values (0.2 to 0.4) represent shrub and grassland, while high values (0.6 to 0.8) indicate forest. The on-site NDVI value was lower, meaning that there was less on-site vegetation than in the surrounding area. There are signs of human activity such as narrow paths in Figure (b), in contrast to the natural montane vegetation shown in Figure (a). Furthermore, these figures show a reduction in vegetation, and we can determine those areas that had changed in that period.

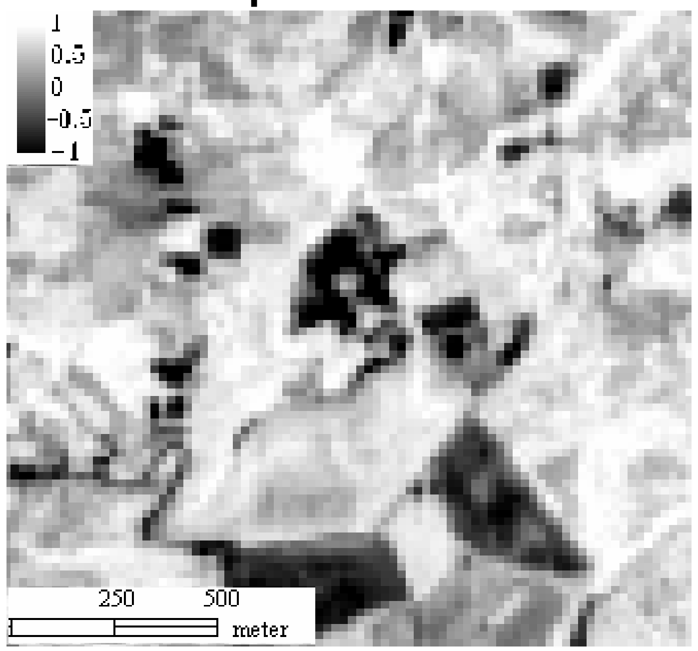

(a) Jul.20, 1992

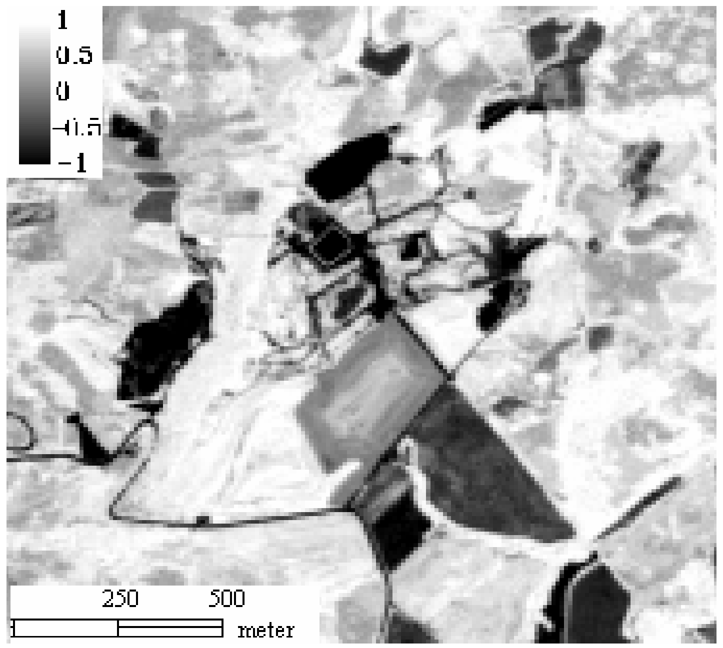

(b) Jun.17, 2004

Changes in NDVI data on the dumping site

Topographic Analysis

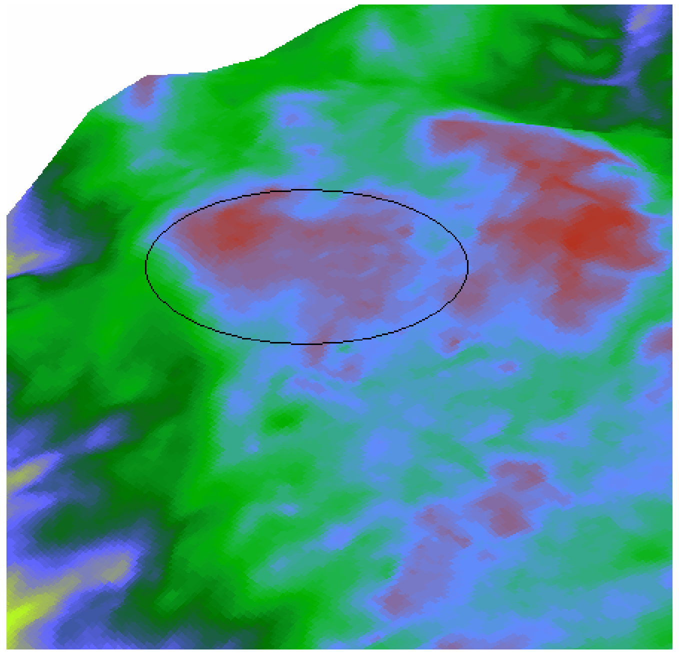

(a) DEM data of 15m spatial resolution

(b) Quickbird data of 2.4 m spatial resolution

(c) Three-dimensional visualization

The DEM data of 15 m spatial resolution was combined with a Quickbird image of 2.4 m spatial resolution to obtain high spatial resolution. The output image is three-dimensional visualization of the illegal dumping site and its surrounding areas.

Water Quality Analysis

Five water quality analyzers have been installed at the former water supply source (Point 1), the new water supply source (Point 2), in the vicinity of the Kumahara River (Point 3), at the intake (Point 4) and the outlet (Point 5) of the water purifying plant. The pH and electric conductivity of on-site water (Point 4 and 5) were higher than normal water (Point 1, 2, and 3), and the pH at Point 4 reduced on rainy days (September 2, 7, 14, and 22).

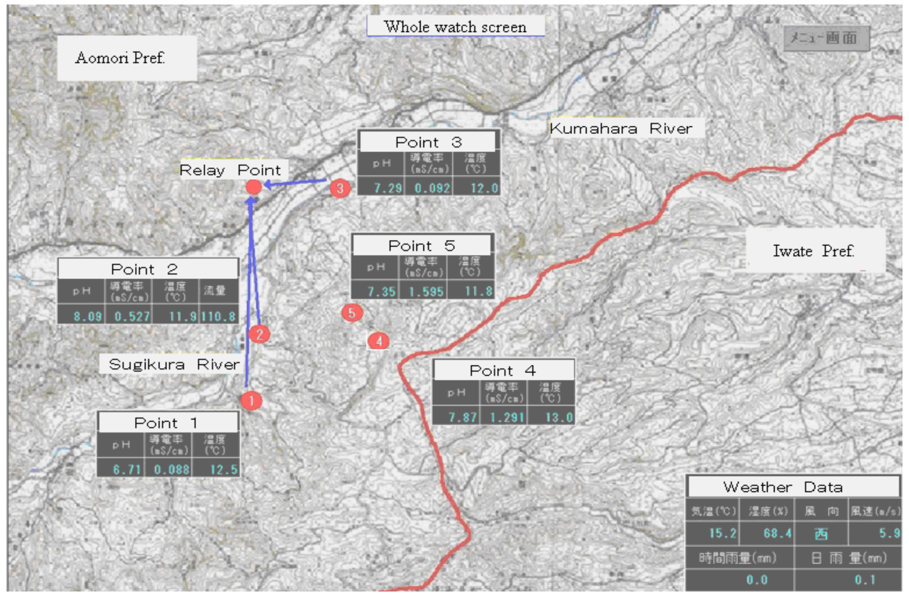

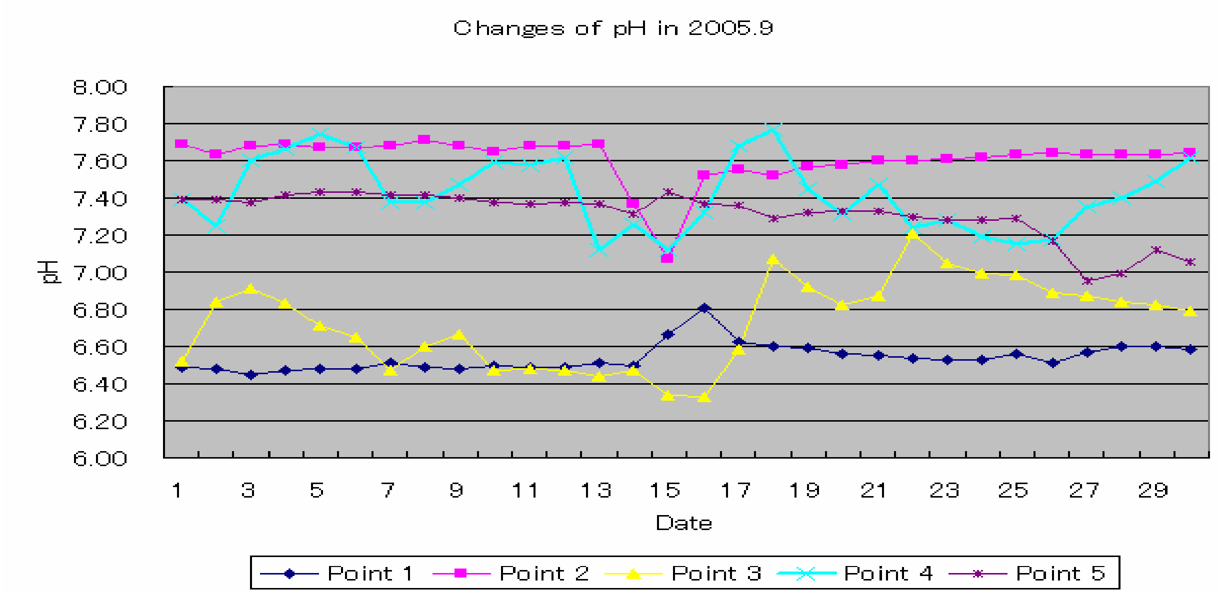

Table 1 Changes in water quality (pH)

	2004.9	2004.10	2005.9	2005.10
Point 3 (Kumahara River)	7.34	7.15	6.93	6.48
Point 4 (entrance of the water purifying plant)	7.92	7.97	7.34	7.58
Point 5 (exit of the water purifying plant)	7.41	7.27	7.18	6.85

34,428 tons of waste (26,668 tons of solid waste and 7,760 tons of fluid waste) was removed. Although only 4% of the total waste in Aomori Prefecture has been removed, almost all the fluid waste has been removed. Furthermore, the extensive work carried out as mentioned above has improved the water quality. We found that the alkalinity of the water was reduced by the water purifying plant — the mean pH in September 2004 fell from 7.92 (Point 4) to 7.41 (Point 5), and in September 2005 fell from 7.34 to 7.18. The mean pH at Point 4 also fell from 7.945 (September and October 2004) to 7.46 (September and October 2005).

Conclusions

A remote sensing system was established to monitor and analyze the environmental data at the illegal dumping site on the border between Iwate and Aomori Prefectures. In this paper, the data collected using this system, including satellite data, images from on-site infrared cameras, and water quality data, was analyzed to establish the level of on-site contamination and state of recovery.

Multispectral SPOT images of high spatial resolution were analyzed using the NDVI to establish changes in vegetation at the dumping site. We found signs of human activity such as narrow paths and a substantial reduction in on-site vegetation when the waste was dumped. This system will help identify and confirm other illegal dumping sites.

Changes in water quality are important in assessing contamination and were analyzed, along with rainfall, as the waste was removed. The removal of waste and other on-site work reduced the alkalinity of the water. In the future, new satellite data and ground data will be sequentially collected by this system. This will be compared with current data to understand and forecast environmental changes.

Processing and interpretation of JERS-1 Synthetic Aperture Radar (SAR) image of Cepu and its surrounding areas, Central Java Province, Indonesia

W.W. Parnadi[1], S. Rusli[1], K. Wikantika[2], J. Tetuko S.S[3]

[1]Department of Geophysical Engineering
Institute of Technology Bandung

[2]Department of Geodetic Engineering
Institute of Technology Bandung

[3]Center for Environmental Remote Sensing,
Chiba University, Japan

Introduction

Interpretation of subsurface condition from Radar image is of great interest, covering surface as well subsurface features with resolution much higher than resolution offered by radar technique. Lithological as well as geological informations extracted from the image could be of higher value. Conventionally, geological features are derived visually from Radar images. Patterns associated with geological structures/features could be detected. Attempts to interpret lithological as well as structural geological features deeper than 1 - 10 meters are of course challenging. We are now in the early stage of our attempts to obtain techniques that make deeper interpretation possible. In this research, we tried to derived geological structures and other features visually from JERS-1 SAR data from Cepu Area, Central Java Province, Indonesia, in which a huge oil reservoir located. Figure 1 and figure 2 show the study area and its geological structures. The use of geological map is intended to get better understanding of geological features and structures that could be recognized in the Radar image. We applied conventional image processing flows on the data to improve data quality that lead to more interpretability of the data.

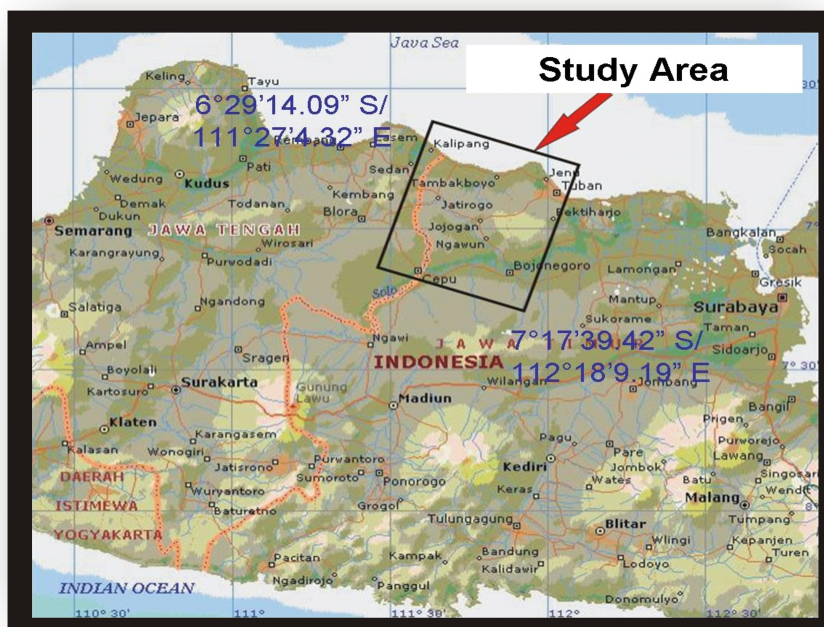

Fig. 1: Cepu Study Area located in Central Java Province, Java Isle, Indonesia

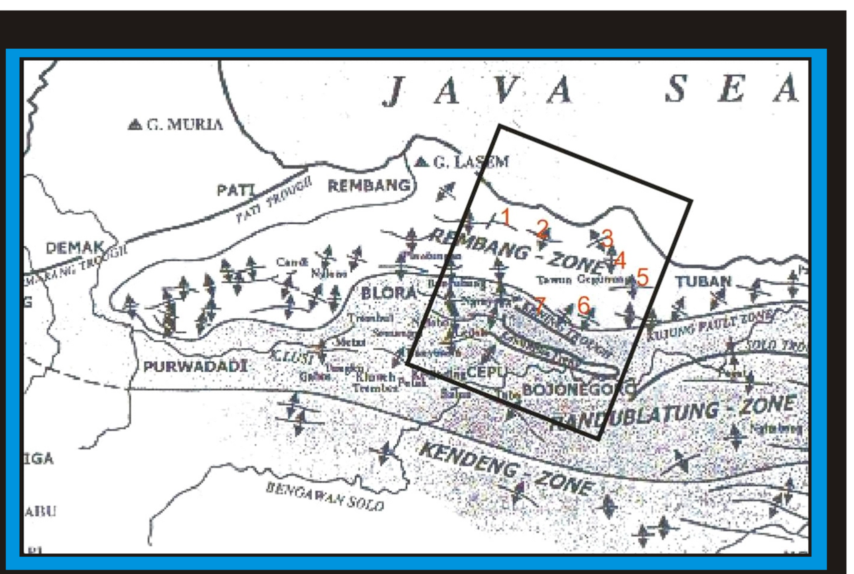

Fig. 2: Geological Structure Map of study area showing anticline folds and their orientations

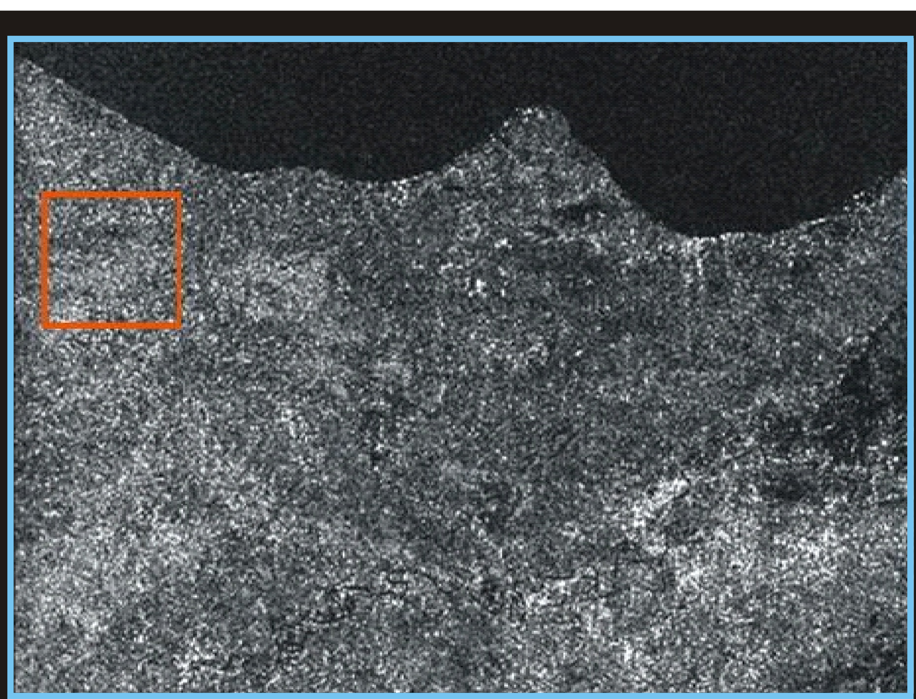

Fig. 3: Raw image of study area. Area for speckle reduction processing step is shown in red rectangle.

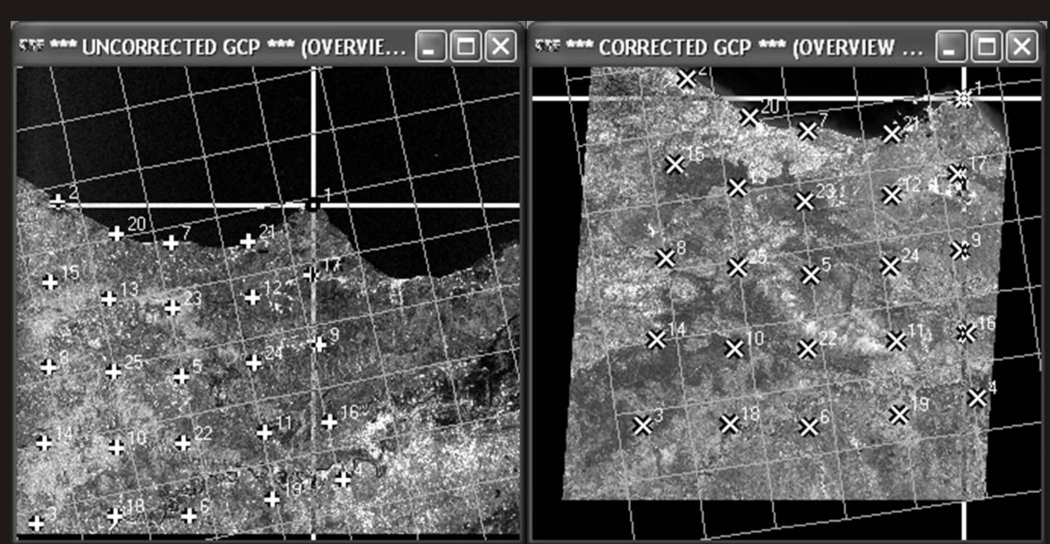

Fig. 4: Distribution of control points in the JERS-1 SAR image (left) and their reference points in the ASTER image (right).

Data and Data Processing

JERS-1 as well as ASTER images for this research were available from Remote Sensing Research Center - Pandhito Panji Foundation and ERSDAC. Combining with data from field observation, we processed the JERS-1 image using following data processing flows: radiometric correction (speckle reduction) with low-pass filtering, geometric correction (image rectification) with least-square polynomial regression, image focusing with linear contrasting and high-pass filtering. All processing steps were conducted using ER Mapper 6.4 software. Figure 3 shows raw image of study area. Rectangle in red denotes area used for comparison in speckle reduction processing step. Geometric correction is applied using JERS-1 SAR and ASTER images. For this purpose, distribution of control points in the JERS-1 SAR image and their reference points in the ASTER image is shown in the figure 4. Figure 5 shows processed JERS-1 image after image focusing. Image histogram after application of high-pass filtering is shown in the right side of the figure. .

References

[1] Darman. H. and Sidi, H. (eds.), 2000. An outline of The Geology of Indonesia : Indonesian Assoc. Geologists (HAGI), Jakarta.

[2] Jensen, J., 1986, Introductory to Digital Image Processing: A Remote Sensing Perspective: Prentice-Hall, New Jersey, USA.

[3] Permana, T. W., 2003, Analysis of Soil Backscattering Value using Transmission Lines Approach and Data Processing of JERS-1 SAR Data (in Indonesian language): BSc. Thesis, ITB, Bandung.

[4] Rimayanti, A., 2001, Geological Mapping with fusion method of SPOT-HRV and JERS-1 SAR Data (in Indonesian language): BSc. Thesis, ITB, Bandung.

[5] Tateishi, R., Al Bilbisi and J. Tetuko S. S., 2003, A Technique to Estimate Topsoil Thickness in Arid and Semi-Arid Areas of North-Eastern Jordan using Synthetic Aperture Radar Data: Int. J. Remote Sensing, **25**, No. 19.

[6] Tetuko S. S., J, Tateishi, R. And Takeuchi, N., 2003, Estimation of Burnt Coal Seam Thickness in Central Borneo using JERS-1 SAR Data: Int. J. Remote Sensing, **24**, No. 4.

Data Interpretation

Processed image combining with geological structures map were available in the interpretation stage. Two types of geological structures were identifiable in the processed image: anticlinal folds and faults. Eleven anticlinal folds and one faulted anticlinal fold were detectable. These folds were identified based on their characteristics, i. e. coarse textures and high brightness values, folded form or horizontally folded and symmetrical or repetitive patterns. Figure 6 shows interpreted anticlinal folds and fault. Blue lines denote fold structures and yellow line denotes shear fault.

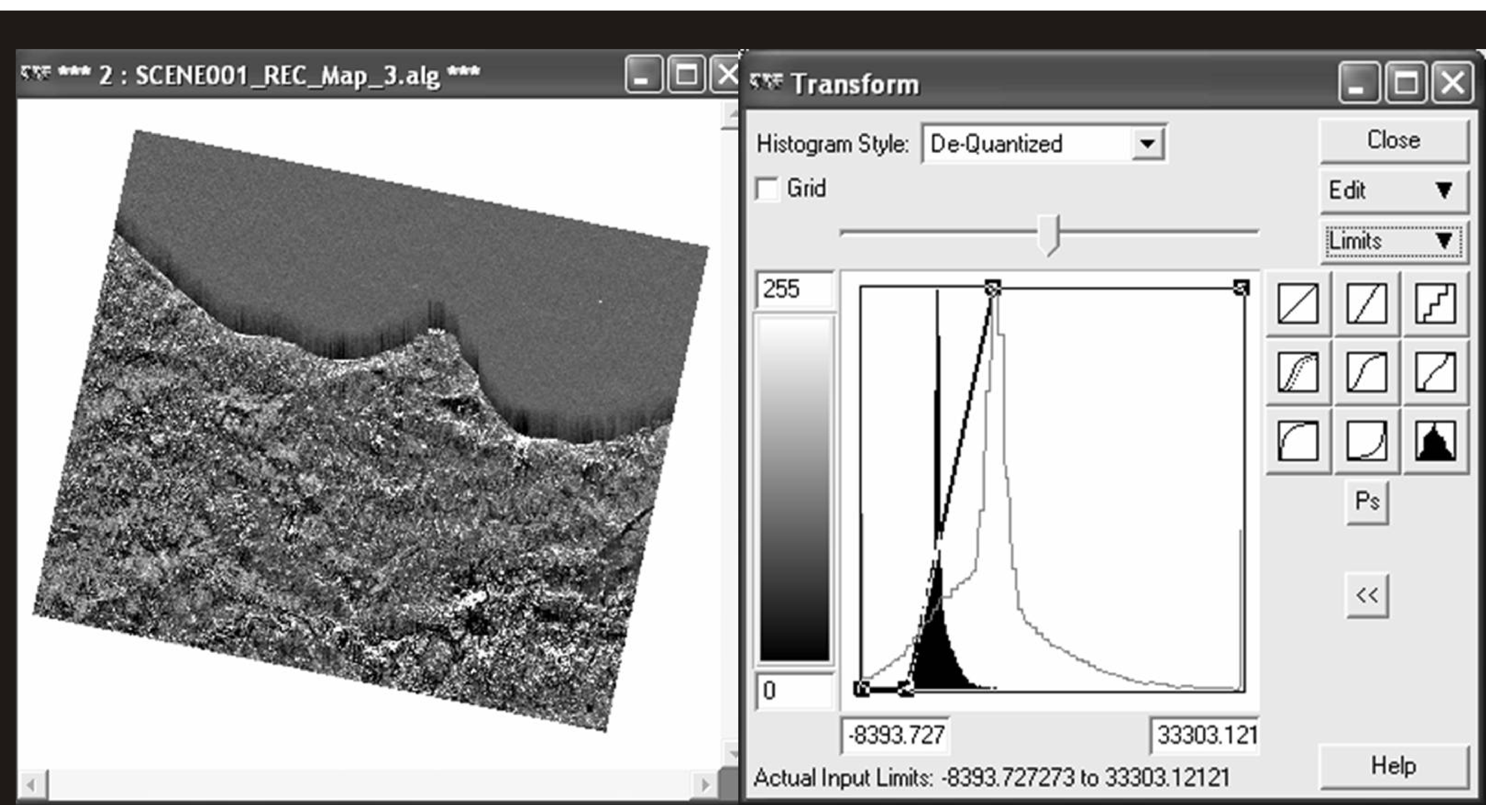

Fig 5: processed JERS-1image after image focusing (left) and an example of applied parameter for image focusing (right)

Shear fault structure was identified based on the appearance of lineaments intersecting folds. Figure 7 is image fraction showing area in the adjacent of interpreted fold no. 1 and shear fault. Symmetrical axes are denoted by blue arrows. These results have been compared with geological structure map. It should be noted that little difference in structure orientation interpretation from image-derived structures and the geological structure map is more likely resulted from the error in the process for geometrical correction, especially for structures located outside ASTER image coverage acting as geometrical correction reference. Moreover, for structures inside the ASTER image coverage, Digital Elevation Modeling (DEM) technique should be incorporated in the processing flows in order to get better results in the determination of structures orientation.

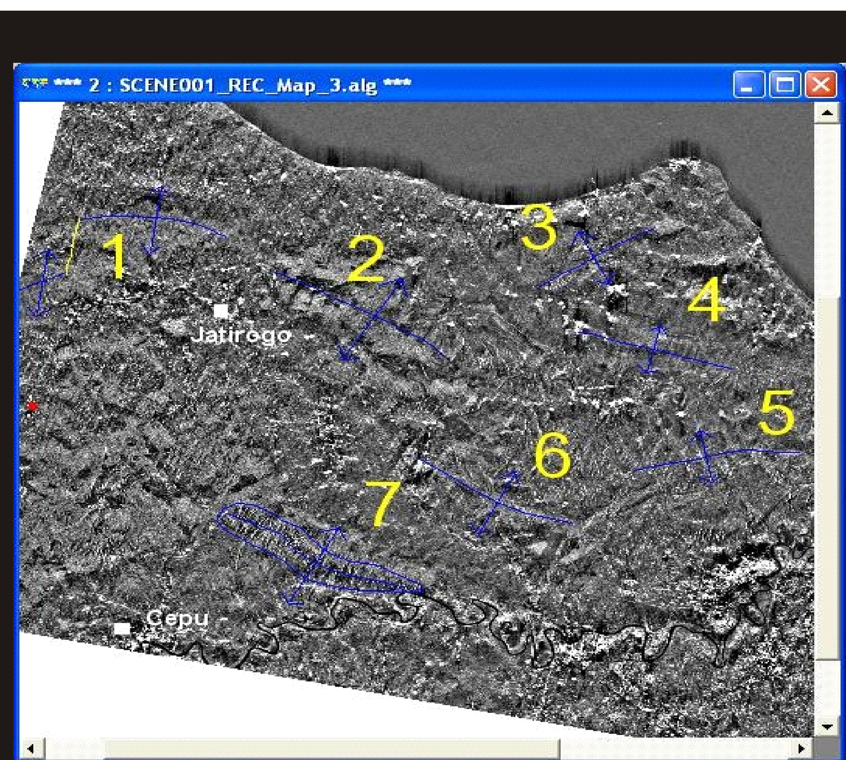

Fig. 6: Interpreted folds (denoted by blue lines) and fault (yellow line) in the study area

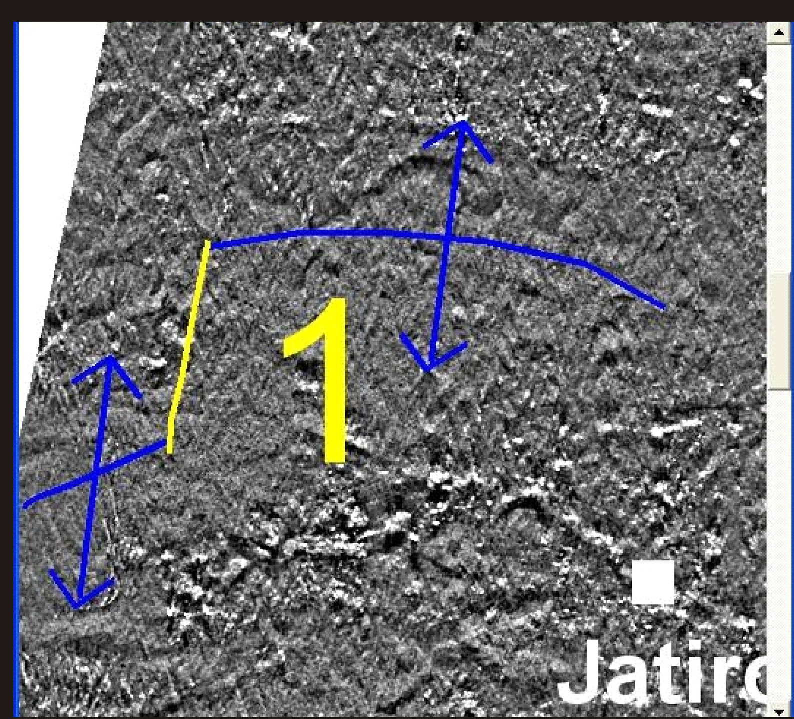

Fig. 7: Image fraction showing more detailed area in the adjacent of interpreted fold no. 1 and shear fault. Arrow signs denote symmetrical axes.

Conclusion

Geological as well as lithological interpretation of subsurface condition from Radar image is of great interest. Conventionally, geological features are derived visually from the images. Patterns associated with geological structures/features are recognized. Attempts to interpret lithological as well as structural geological features deeper than 1 10 meters are of course challenging. This research is in the early stage of an attempt to derived lithological and geological features from Radar image conducted in the Department of Geophysical Engineering of Institute of Technology Bandung, Indonesia. In this stage, we tried to derived geological structures and other features visually from JERS-1 SAR data from Cepu Area, in which a huge oil reservoir located. Conventional image processing flows applied on the data could improve data quality that lead to more interpretability of the data. Eleven anticlinal folds and one faulted anticlinal fold were detectable. These folded could be identified based on their characteristics: coarse textures and high brightness values, folded form or horizontally folded and symmetrical or repetitive patterns. Shear fault structures could also be identified based on the appearance of lineaments intersecting folds. A little difference in structure orientation interpretation from image-derived structures and the geological structure map could be resulted from the error in the process for geometric correction, especially for structures located outside ASTER image coverage acting as geometrical correction reference. Even for structures inside the ASTER image coverage, Digital Elevation Modeling (DEM) technique should be incorporated in the processing for better results in the determination of structures orientation.

Acknowledgement

We thank Remote Sensing Research Center - Pandhito Panji Foundation and ERSDAC of Japan for providing the JERS-1 SAR and ASTER image data.

#15

Comprehensive evaluation of Leaf Area Index estimated by several method — LAI-2000, SunScan, Fish-eye, and littertrap —

Midori Kurata[1] , G.A.Sanchez-Azofeifa[2] , Wang Quan[1] , Yoshitaka Kakubari[1]

1 Faculty of Agriculture, Shizuoka University , 2 Earth & Atmospheric Sciences University of Alberta,Canada

E-mail： zoorin@agr.shizuoka.ac.jp

1) Introduction

Leaf Area Index (LAI) is a key biophysical variable influencing land surface processes such as photosynthesis, transpiration, and energy balance and is a required input for various ecological models. It is necessary to rely first on ground-based LAI estimates if remotely sensed vegetation indices need cross-calibration. At present, there are several techniques for estimating LAI. The aim of this study is to establish a practical technique for LAI estimation suitable to mountaineous beech forest stands.

2) Material & Method

Study site ・The northern slope of the Naeba Mountain (36° 51'N, 138° 41'N), located in southern Niigata Prefecture in Japan

・dominant species is beech (*Fagus Crenata*)

type	old-beech							mix-wood					young-beech	
site name	1500k	1500y	1300y	900X3	700n2	600k	550k	1200y	1100y	900y	900X4	700n	900X1	900X5
altitude (m)	1500	1500	1300	900	700	600	550	1200	1100	900	900	700	900	900
age of stands (yr)	300	300	300	150	200	250	260	250	250	250	150	200	70	85
DBH (cm)	17.6	13.8	11.5	28.9	36.9	30.2	37.1	20.0	11.8	16.6	15.8	16.0	23.1	17.3
mean tree height (m)	22	20	20	22	30	27	34	20	19	31	21	31	21	21
stand density (trees ha-1)	450	229	250	383	361	433	246	539	625	535	829	425	1033	1400
basal area (m2/ha)	30.4	21.3	31.4	41.6	52.4	45.6	36.3	35.3	53.8	44.8	30.8	30.9	51.1	46.5
percent of Fagus Crenata (%)	71	72	86	59	82	74	86	33.0	38.0	41.0	28.1	31.4	94	74
	○	○	○	○			○		○	○		○		

○; destructive sampling were made in 1970s

Mt.Naeba (2145.3 m)

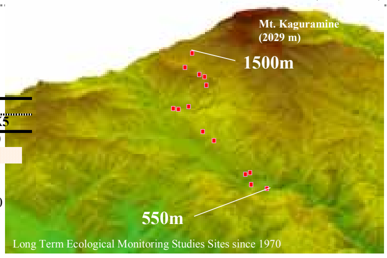

3) Estimating LAI by direct methods

litter collection

5-10 litter traps were set randomly at 8sites respectively

allometric aquation In seven sites, destructive samplings were made for parameterising allometric at each altitude (IBP, 1970)

log F = h log (D²H) + K ･･･ (for old-beech and mix-wood)

F = 0.006 × (Dπ)²+ 0.4656 (Dπ) ･･･ (for young-beech)

F: total leaf area of each tree, D: diameter at breast height, H: tree height, *h* and *K:* fitted coefficients of the equation at different altitudes.

4) Estimating LAI by indirect methods

measuring radiation based on gap fraction and calculating LAI from the Beer-Lambert extinction law

LAI-2000 :The Plant Canopy Analyser (LI-COR Inc. , USA) measure the diffuse radiation below 490nm. In this study, with view caps of 22.5° and 90°

SunScan：Canopy Analysis System (Delta-T Devices Ltd, UK) measure the PAR above canopy (with BFS) and below canopy (with probe)

} measure both **incoming radiation** and **transmitted** through the canopy

Fish-eye

Hemispherical photograghs taken by using digital cameras with →calculated by a specific software Hemiview (Delta-T Devi er). (gap fraction and canopy openness)

3) Results and Discussion

1) Estimated LAI by direct methods

.·litter collection: One of the most reliable methods the LAI estimation

● For the old-beech forest, the relationship was almost 1:1

● The destructive sampling was made for sites with no litter traps, from which the estimated values then used as ground truth

In this study, LAI from litter collection or allometric equation was treated as true values,

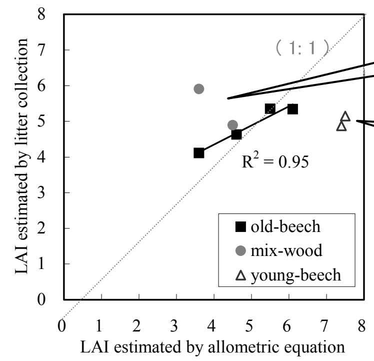

Fig. 1 Relationships between LAI estimated by allometric equation and by litter collection.The dotted line is 1:1

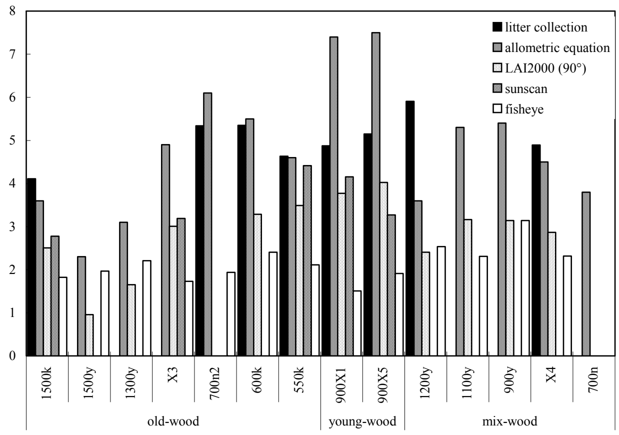

Fig. 3 LAI Estimated by litter collection, allometric equation, LAI-2000, SunScan and Fish-eye.

Among these indirect methods,

LAI-2000 has the strongest correlation with the direct estimated LAI.

with 90° view-cup → Wide field-of-view is much desired for the heterogeneous radiation environment as below canopy.

Although it was underestimated →It needs connection before it can be used.

SunScan estimated LAIe of old-beech has the linear relationship to direct LAI, although in young-beech LAIe was underestimated.

Fisheye estimated LAIe is saturated around LAIe =2. Classification of images involves using digital image process to distinguish canopy opening from foliage, which is achieved by determining a threshold intensity value.

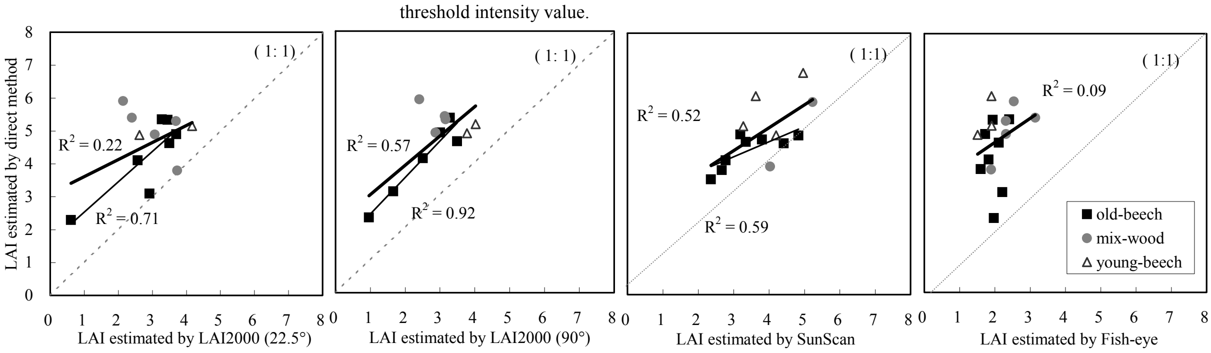

Fig. 2 The relationships between LAI based on direct methods and LAIe estimated by LAI-2000, SunScan and Fish-eye. Thick line shows the correlation of all samples, while thin line only for old-beech.

4) Conclusion

LAI-2000 was suitable for LAI estimation in mountain beech forests.
And broad view angle is required for measuring. In addition, it usually underestimates LAI and thus needs conection before it can be used.

Although it is very portable, Fish-eye measuring requires more technique.

SunScan is hard to use in the forest stands if the cable is connected to BFS. However, SunScn is resistant to weather changes and can keep measuring under versatile weather conditions.

APPLYING THE REMOTE SENSING IN A DECISION SUPPORT TOOL FOR FOOD SECURITY

ELEONORA RUNTUNUWU, SETYONO HARI ADI, and FADHLULLAH RAMADHANI
Indonesian Agroclimate and Hydrology Research Institute
Email: runtunuwu2000@yahoo.com

1. INTRODUCTION

1. One of the most significant challenges for improved the national food security program is availability of timely, up-to-date, and accurate data for planners and decision makers. Such information needs to be available to concerned government official, regulators, donors, NGO and other interested organizations in a comprehensive, consistent, regular, and easy to understand format.
2. In Indonesia, there are many institutions concerned in food security data, which each institution has own analytical tools and methods for determining the food security parameters; therefore, we often find a dissimilar published data for a same physic variable such as the paddy field area of a certain province. In addition, it takes time for collecting the historical data from local until national levels; consequently, it is awfully difficult to access the real time food security information.
3. This research attempts to (1) develop a food security database system included an analytics instrument to improve the quality of paddy field data using remote sensing and GIS technologies, (2) calculate the food balance of each region using DSS model, and (3) design the food security information system.
4. All kind of spatial data either image or vector as well tabular data have been integrated in a database system, and then transformed into food security information to enhance the knowledge based as a basis for decision making are discussed in this paper

2. HOW TO ACHIEVE THE GOAL AND SATELLITE IMAGE USED IN THIS STUDY (CASE STUDY: MIDDLE OF JAVA PROVINCE)

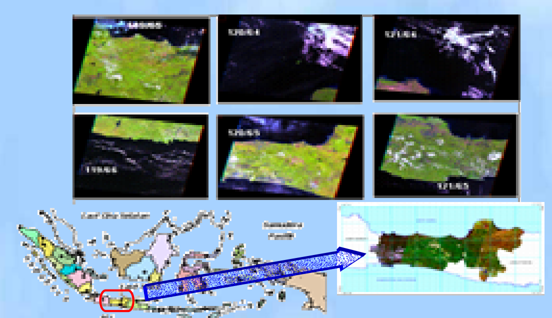

3. ANALYTICS INSTRUMENT TO DETERMINE PADDY FIELD AREA ON FOUR CLASSES OF SLOPE

4. REGRESSION ANALYSIS OF (A) RS VS THEODOLITE AND (B) RS VS GPS BASED ON FOUR CLASSES OF SLOPE

(A) RS VS Theodolite

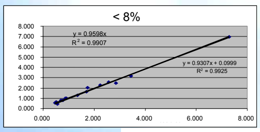

(B) RS VS Theodolite and GPS VS Theodolite

No	Slope (%)	a constan		Corelation Coeficeint (R^2)	
		RS	GPS	RS	GPS
1.	< 8	0.9598	0.9667	0.9907	0.9874
2.	8 - 16	1.0956	1.1072	0.7891	0.8106
3.	16 - 45	0.9419	1.0588	0.9658	0.9307
4.	> 45	0.9713	0.9242	0.6116	0.7710

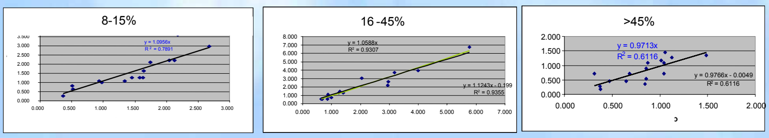

RS = remote sensing: GPS = global positioning system

5. ESTIMATION OF PADDY YIELD (KG) USING PADDY FIELD AREA (HA) AND PRODUCTIVITY (KG/HA)

NO	Location	Distric	Slope (%)	GPS (ha)	Theodolite (ha)	RS (ha)	Paddy yield (kg)
1	Dukuh Karya	Karawang	0-8	6.960	7.295	6.972	393.74
2	Karya Mulya	Karawang	0-8	2.456	2.865	2.477	143.85
3	Karang Jaya	Karawang	0-8	1.880	1.735	2.018	101.49
4	Pagadungan	Karawang	0-8	2.503	2.247	2.293	127.41
5	Ciranggon	Karawang	0-8	2.603	2.565	2.569	166.66
6	Campaka	Purwakarta	8-15	0.510	0.520	0.642	38.06
7	Cikumpay	Purwakarta	8-15	2.312	2.125	2.202	130.55
8	Nagri Tengah	Purwakarta	8-15	1.787	1.745	2.110	125.09
9	Sawah Kulon	Purwakarta	8-15	2.024	2.045	2.202	130.55
10	Pasawahan	Purwakarta	8-15	1.523	1.625	1.260	74.70
11	Kerta Mukti	Padalarang	16-45	2.272	2.055	3.060	181.41
12	Karang Layung	Padalarang	16-45	1.404	1.395	1.260	74.70
13	Babakan Sari I	Purwakarta	16-45	0.830	0.895	0.900	53.36
14	Sampay	Cianjur	16-45	1.341	1.255	1.260	74.70
15	Warung Jambe	Padalarang	16-45	2.308	2.945	2.160	128.06
16	Cikondang	Padalarang	>45	1.216	1.125	1.260	74.70
17	Babakan Sari II	Purwakarta	>45	0.281	0.375	0.270	16.01
18	Lingga Mukti I	Purwakarta	>45	0.593	0.645	0.450	26.68
19	Lingga Mukti II	Purwakarta	>45	0.425	0.475	0.450	26.68
20	Marga Asih	Padalarang	>45	0.516	0.685	0.720	42.69

6. FOOD BALANCE USING DSS MODEL

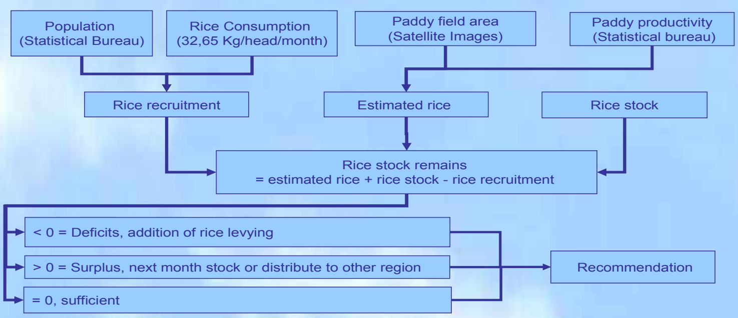

7. DEVELOPMENT OF WEB-BASED FOOD SECURITY INFORMATION SYSTEM

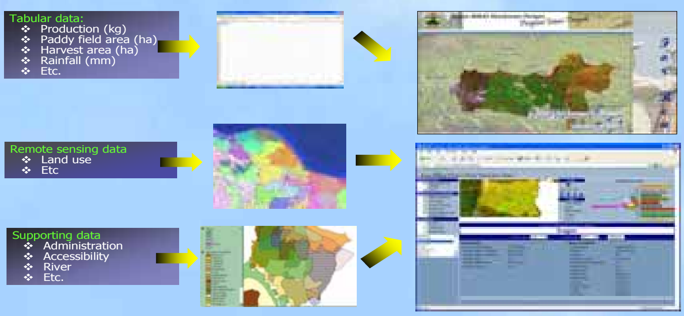

8. CONCLUSIONS

Food security has to be achieved at national, local and household levels by securing the access to food by the population and to information by policy makers. The decision support system (DSS) for food security that has been developed for Central Java province was carried out in three main phases: i. e.

(a) identify and develop required variable in the food security database such as demographical, statistical, satellite data, etc;
(b) estimate paddy production of each district using high resolution images and compute food balance based on the supply and demand, and
(c) design and operate the information delivery system to multiple users.

With the DSS the different variables and criteria commonly used by various institutions dealing with food security can be standardized. The utilization of multi-spectral and multi-temporal satellite imagery integrated in geographic information system as components of the DSS will facilitate the efforts of all the institution as well as minimizing the cost.

Experimental study on the effect of Cheong-gye stream restoration on urban environment

(Long-path measurement of atmospheric pollutant species with an obstruction flashlight)

Yohei Shiraki, Ippei Harada, Hiroaki Kuze(CEReS, Chiba University)
Toshiaki Ichinose(Center for Global Environmental Research,National Institute for Environmental Studies)
Yingjiu Bai(Tohoku University of Community Service and Science)

Purpose

The expressway was dismantled in Seoul in July, 2003, and the municipal river (Cheong-gye stream) was restored in October, 2005.

In this study, It is intended that the atmospheric pollutant data and the air temperature data are accumulated in the proof of the relaxation effect of the heat island phenomenon in Cheongegecheon.

Study Area(SEOUL)

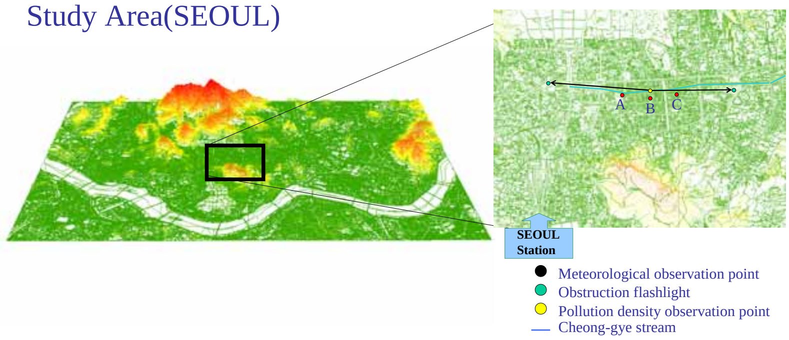

Research method

1) Long-path measurement of atmospheric pollutant species with an obstruction flashlight
2) Observation of air temperature

Observation technique of atmospheric pollutant species

1)The background from the sky radiation is easily subtracted because the spectra of strobe flash are distinguished straightforwardly from the difference of the observed intensity.

2)simultaneous observation of several trace gas species is feasible if the relevant spectral features fall within the considered wavelength interval of the lamp and the CCD.

3)when the spectral intensity of the flashlight is known at the strobe site, the transmitted spectra give an information on the aerosol extinction along the optical path.

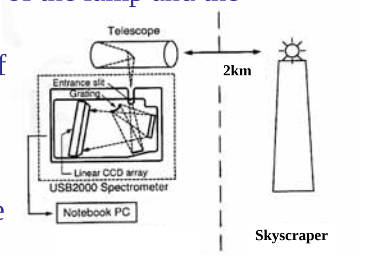

Fig1. Experimental setup for measuring NO_2.

Result of observation Air temperature

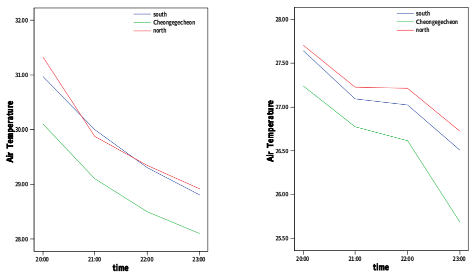

Fig2. daily variation of air temperature(Left:2004, Right:2005)
(North-South)

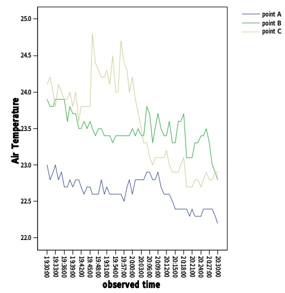

Fig3. daily variation of air temperature
(East-West)

Future work

The atmospheric pollutant species observation and the meteorological observation in Seoul will be studied, and the relaxation effect of the heat island phenomenon of the municipal river will be clarified.

Thus, it is possible to contribute to the creation of the municipal river and the promotion of maintenance in Asian cities.

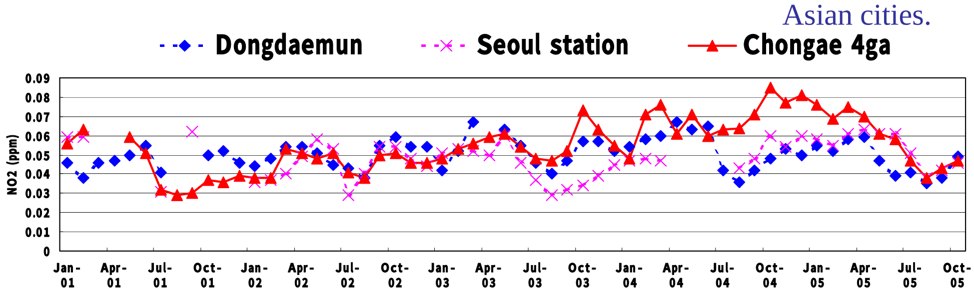

Fig3. Secular distortion of NO_2 measured around road

As for the rise of NO_2 in Chongae 4ga,2004, The influence of construction is stronger than the influence of the autoexhaust.

It is worth observing atmospheric pollutant species .

Cheong-gye stream (August 2004)

Cheong-gye stream (September 2005)

Pollution density observation point

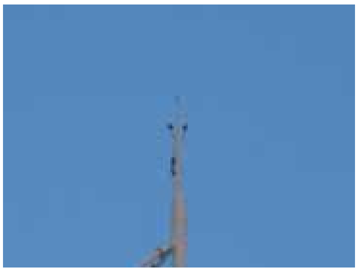

obstruction flashlight

Study the effect of green covering on the land value of Tokyo Metropolis using geographic information system (GIS)

Ippei Harada (Graduate school of Science and Technology, Chiba University)
Akihiko Kondoh (Center for Environmental Remote Sensing, Chiba University)

Background

The urbanization around the center of Tokyo was expanded due to the increasing population of the Tokyo region (Tokyo, Chiba prefecture, Saitama prefecture, Kanagawa prefecture). The housing establishment and city traffic have developed the suburbs which were before an agricultural land and mountain area. The rapid expansion of Tokyo region from the end of 1980s till the beginning of 1990s was due to the impact of the economic bubble, which consiquence, increased the land and stock values, thus increased the problem of urban environment.

Land value is a quantified economic parameter which shows the utility value of land. It is a comprehensive value which reflects the environmental condition and many other functions of the city.

Study Area

The extent of Tokyo metropolis is about 100 km and there are many cities existed also on the fringe of Tokyo. Tokyo is the center of major activities and developments of Japan. The impacts of the urbanization was not limited in Tokyo area but it was extended also outside Tokyo region to include the nearby prefectures, which then increased their land prices.

Fig 1. Tokyo region

Data

- 10m Grid Land Use:Metropolitan Area (in 1984 and 1994) .
- 2 scenes of Landsat TM data acquired during daytime August 3,1985 and July 19,1997 (Path：107 / Row：35) .
- Official announcement of land price in 1985 and 1997.
- Land classification map at 1:500000 scale (Chiba, Saitama, Tokyo and Kanagawa prefecture → Tokyo region) .

Research method

1) The city environmental element was extracted using Geographical Information System (GIS).
2) The influence of the city environmental element was correlated with the formation of land values and analyzed using multiple linear regression analysis.

Land use/cover change during the bubble economic term

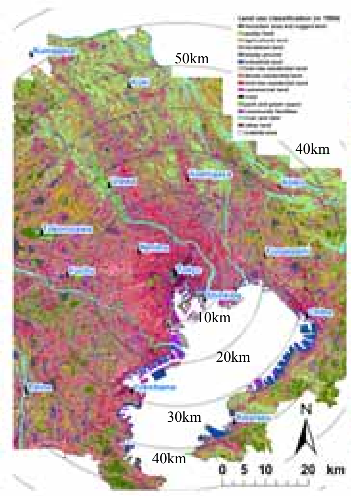

Fig 2. Land-use of Tokyo Metropolitan in 1984.

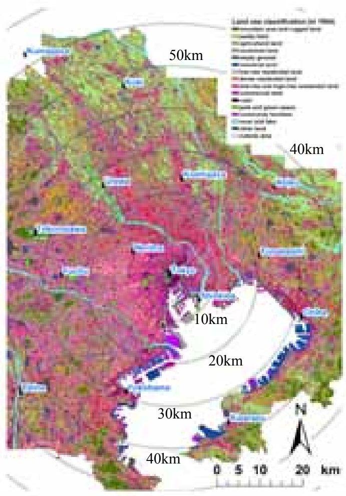

Fig 3. Land-use in the Tokyo Metropolitan in 1994.

Table 1.The percentage of changes of land use from 1984 to 1994.

Land use	Chiba	Saitama	Tokyo	Kanagawa
Mountain district Paddy field Agricultural land	-3.26	-4.23	-2.31	-2.58
Park Green space	0.46	0.48	0.50	0.35
Reclaimed land Road Community facilities	1.53	0.84	1.08	0.98
Industrial land Residential land Commercial land	1.95	2.39	1.82	1.74

Artificial land use was increased in Tokyo region. Natural land use was decreased in Tokyo region. However, park and green space were increased.

The center of Tokyo → Land use change is small

The suburbs → Land use change is large

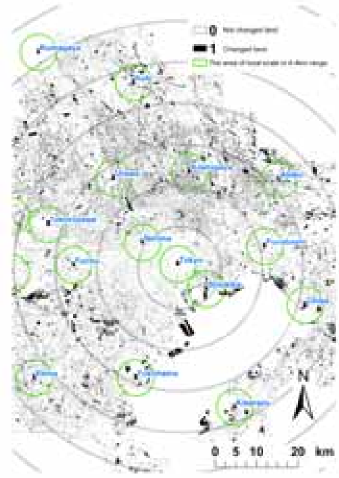

Fig 4. Land-use change of Tokyo Metropolitan during the period (1984-1994).

Multiple linear regression analysis

Land value

p(z) =f＊(Z1+Z2+,･･･,Zn) ← Extracted using GIS

Z1: Spatial distance from Tokyo station, Z2:Spatial distance up to near station → convinience

Z3:Building structure（reinforced concrete, steel framework, timbered) → safety

Z4:With or without of Town gas, Z5: With or without Sewerage, Z6: With or without Water supply → economical efficiency

Z7:Land area, Z8:Building coverage ratio, Z9:Building capacity ratio, Z10:Land form（hillyland, upland, lowland, reclaimed land）, Z11: Green covering ratio → amenity

Table 2. Determining factors of land values by regression analisis of the meso-scale

Multiple linear regression analisis (Land value in 1984 and in 1997)		
Year	in 1985	in 1997
Explaining variable 1	Spatial distance from Tokyo station	Building capacity ratio
Explaining variable 2	Sewarage	Spatial distance from Tokyo station
Explaining variable 3	Spatial distance up to near station	Sewarage
Explaining variable 4	Land form（hillyland>upland>lowland>reclaimed land）	Spatial distance up to near station
Explaining variable 5	Town gas	Building structure（reinforced concrete>steel framework>timbered）
Explaining variable 6	Building coverage ratio	Land form（hillyland>upland>lowland>reclaimed land）
Explaining variable 7	Building structure（reinforced concrete>steel framework>timbered）	Building coverage ratio
Explaining variable 8	Building capacity ratio	Town gas
Explaining variable 9	Green covering ratio	Green covering ratio
Multiple correlation coefficient	0.647	0.794
Contribution ratio (%)	64.4	63.0

NDVI
= (NIR(TMband4)－Red(TMband3)) / (NIR(TMband4)＋Red(TMband3))

↓

Vegetation region：0.1<NDVI
The area of local scale in 4.4km range from the city

Tokyo city (in 20km range from the center of Tokyo) :
Nerima, Tokyo(Otemachi), Shinkiba

Around Tokyo city (in 20～30km range from the center of Tokyo) :
Funabashi, Urawa, Koshigaya, Fuchu, Yokohama

Suburban 1 (in 30～40km range from the center of Tokyo) :
Abiko, Chiba, Kisarazu, Tokorozawa

Suburban 2 (in 40～50km range from the center of Tokyo) :
Kumagaya, Hatoyama, Kuki, Hachiouji, Ome, Ebina

Table 3. Determining factors of land values by regression analisis of the rocal-scale

Multiple linear regression analisis (Land value in 1985)				
	Tokyo city	around Tokyo citty	Suburban 1	Suburban 2
Explaining variable 1	Spatial distance from Tokyo station	Sewarage	Sewarage	Green covering ratio
Explaining variable 2	Green covering ratio	Spatial distance up to near station	Spatial distance up to near station	Sewarage
Explaining variable 3	Building capacity ratio	Green covering ratio	Land form	Spatial distance up to near station
Explaining variable 4	Building coverage ratio	Town gas	Building structure	Land area
Explaining variable 5	Spatial distance up to near station	-	Building capacity ratio	Building coverage ratio
Explaining variable 6	Land area	-	Green covering ratio	Building structure
Explaining variable 7	-	-		Spatial distance from Tokyo station
Explaining variable 8	-	-	-	Town gas
Multiple correlation coefficient	0.647	0.708	0.861	0.842
Contribution ratio (%)	28.3	48.6	71.4	67.3

Multiple linear regression analisis (Land value in 1997)				
	Tokyo city	around Tokyo citty	Suburban 1	Suburban 2
Explaining variable 1	Building capacity ratio	Building capacity ratio	Sewarage	Building capacity ratio
Explaining variable 2	Spatial distance up to near station	Spatial distance up to near station	Building capacity ratio	Green covering ratio
Explaining variable 3	Building structure	Green covering ratio	Spatial distance up to near station	Sewarage
Explaining variable 4	Green covering ratio	Sewarage	Green covering ratio	Building structure
Explaining variable 5	Land form	Land form	Spatial distance from Tokyo station	Spatial distance up to near station
Explaining variable 6	Land area	Building structure	Building structure	Spatial distance from Tokyo station
Explaining variable 7	-	Building coverage ratio	Building coverage ratio	Town gas
Explaining variable 8	-	Town gas	Land form	Land area
Explaining variable 9	-	Spatial distance from Tokyo station	-	Building coverage ratio
Explaining variable 10	-	-	-	Land form
Multiple correlation coefficient	0.894	0.883	0.861	0.842
Contribution ratio (%)	79.5	77.4	71.4	67.3

Conclusions

Multiple linear regression analysis was used to analyze the effect of the green environmental impact on the formation of land value. It was not be able to explain the influence of the vegetation impact on the land value of the area through the meso-scale in 70km range from the center of Tokyo, but this influence was clarified through the area of local scale in 4.4km range from the city of Tokyo metropolis as considered one of the elements that the vegetation could influence the formation of land value.

The relationship between PAL NDVI and land use changes in semi-arid regions, China

Hajime OSADA (Graduate School of Science and Technology, Chiba University)
Akihiko KONDOH (Center for Environmental Remote Sensing, Chiba University)

Objective

・To discuss the relationship between remote sensing data and land use/cover changes.
・To evaluate whether it is suitable for which indicator expressing the kind of environmental change in semi-arid regions.

Study area

・110～125° E, 40～55° N.
・It was mainly located in the semi-arid regions, northeast part of China .
・The Grassland occupies the greatest portion of land cover in this area.
・The grassland of the semi-arid regions tend to be influenced by the human-driven factor and the climate-driven factor.

Figure 1. Study area

Data

Pathfinder Advanced Very High Resolution Radiometer Land Data Set (PAL)

・Instrument: NOAA/AVHRR
・Temporal resolution: 10-day
・Spatial resolution: 0.1°
・Period covered: 1982-1999

Land use map

The source of land use information is Land use map of China, 1:1000000 and 1km mesh Land-use map of China. Both maps were made by Chinese Academy of Science, and they have different period covered (table 1). Since the names of the types in the two maps were different, they were classified into six types which unified both (table 2).

Table 1. Property of land use maps

Name	Period covered	Number of land use types
Land-use map of China, 1:1000000, (1980s)	1978-1987	52 layers
1km mesh Land-use map of China(Later 1990s)	1996-2000	25 layers

Table 2. Fusion of land use types of different two maps

Land use types	Land-use map of China, 1:1000000, (1980s)	1km mesh Land-use map of China (Later 1990s)
Cultivated land	Paddy, Irrigated field, Non-irrigated field, Garden	Paddy, Field
Forest	Timber forest, Economic forest	Forestland, Shrub, Sparse forest, other forest.
Grassland	Pastureland, Meadow, Steppe	High, middle, and low coverage grassland
Unused land	Sandy land, Sandy desert, Gobi, Saline-alkali land	Sandy land, Sandy desert, Gobi, Saline-alkali land, Bare land
City, Industrial area, Habitat	City, Town, Industrial and mining area	City, Habitat of farmer, Other building site
Water	River, Lake	River, Lake, Dam, Sandy Shore

Long term change analysis (Large scale)

Indicators for environmental change detection

・NDVImax: Annual max value of NDVI(Normalized Difference Vegetation Index).
It means annual max production of vegetation.
・iNDVI: Annual integrated value of NDVI.
It means annual biomass of plants.
・Tmax: Annual surface temperature.
Surface temperature was calculated by using split window method from channel 4 and channel 5.
・TRJ: Annual slope of trajectory on Ts(surface temperature)-NDVI space.
This shows the reaction which changes with land cover types change. It shows small value on forest and high value on grassland.

・The trend maps of NDVImax and iNDVI may show that annual production of vegetation in most areas tend to increase.
・The distribution of negative trend of TRJ is correspond with positively indicating trend of NDVImax and iNDVI.

The extracted are showing characteristic trend which was compared with PAL NDVI and land use/cover change on local scale.

Extract the area showing characteristic trend

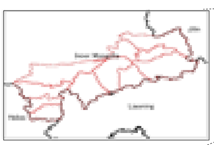

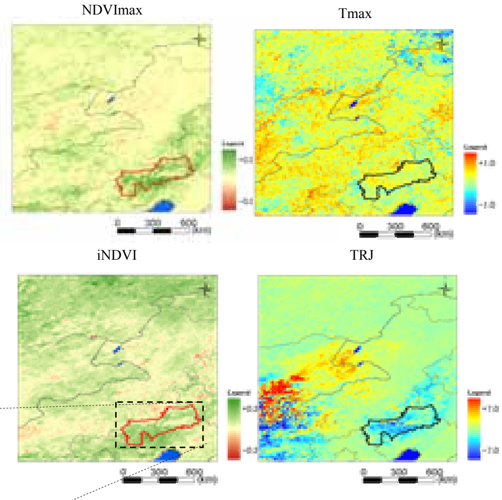

Figure 2.Trend of indicators, 1982-1999

The relationship between PAL data and land use/cover change (Local scale)

Land use change

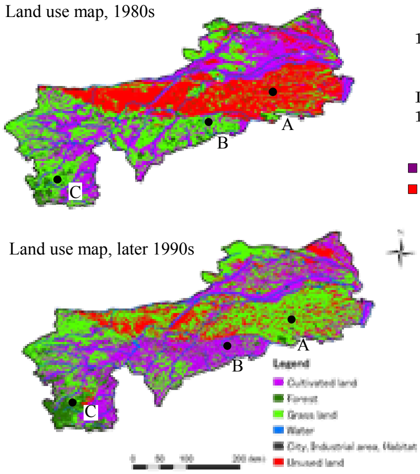

Figure 3. Land use map of 1980 and later 1990s.

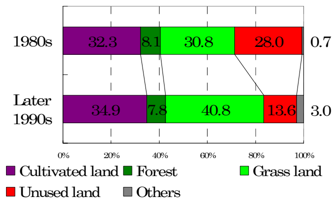

Figure 4. Composition of land use types, 1980s and later 1990s.

Overall trend

・It was guessed that Almost 10 % of unused land changed to grass land.

Characteristic region

・Central area (on the fringe of point A)
Unused land → Grassland
・South area (on the fringe of point B)
Grassland → Cultivated land
・Southwest area (on the fringe of point C)
Grassland → Forest

Comparison of PAL NDVI and land use/cover change

・NDVImax is sensitive to land use changes in the 3 point.
・iNDVI is less sensitive to land use in point A (Unused land → grassland) and point B (grassland → cultivated land). It can express the change of grass to forest in point C.
・Tmax shows similar trend of temporal change, so it may react to annual climatic variation.
・TRJ is sensitive to land use change in point A and B.

The temporal change pattern which was alike at 3 different points was shown. This was considered to be influenced of a climate change.

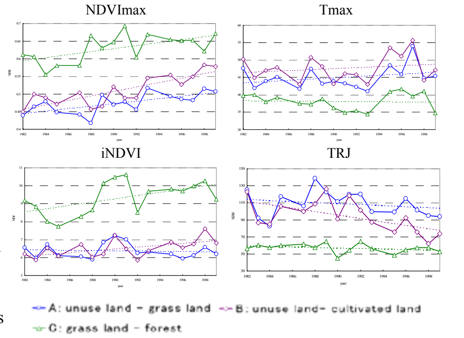

Figure 5. Temporal changes of indicators at the 3 points on fig 4. Broken line shows regression line.

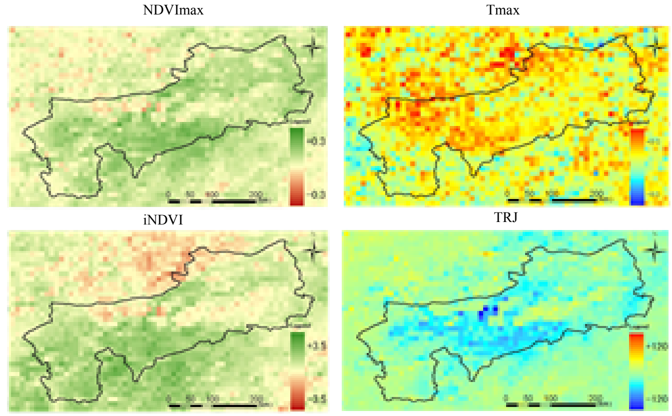

Figure 6. Difference of the average value of indicators between 1982-1987 and 1996-1999. Positive value means increasing and negative value means decreasing.

・All indicators except Tmax show the signal of the change to cultivated land from grassland on south part.
・On the area changed from unused land to grassland, all indicators didn't show characteristic trend.
・Because coincidence of a distribution with land use change was not obtained, this was considered that factors other than the human-driven factor have influenced strongly.

Conclusion

・In this study, the changes of the land use/cover in the local scale were detected using PAL NDVI data.
・It was strongly found that the human-driven factor has more effect than the climate-driven factor.

The characteristics of water resources in XinJiang Uyghur Autonomous Region,China, using GIS and remote sensing

Dilnur Aji [1], Akihiko Kondoh [2]

[1]Graduate School of Science and Technology, Chiba University

[2]Center for Environmental Remote Sensing, Chiba University

Introduction

Lakes and rivers are the most important water resources in XinJiang, since there are little precipitation and melted-snow water from high mountains, which are limited in summer season. The characteristics of water resources and the cause of these changes was analyzed in this research.

Objectives

. To detect the water area fluctuation of main lakes

. To explore the rivers outflow change in the last 50 years

. To analyze the main factors that governing water resources

Study area

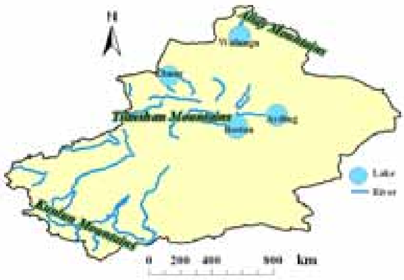

Used Data and Methodology

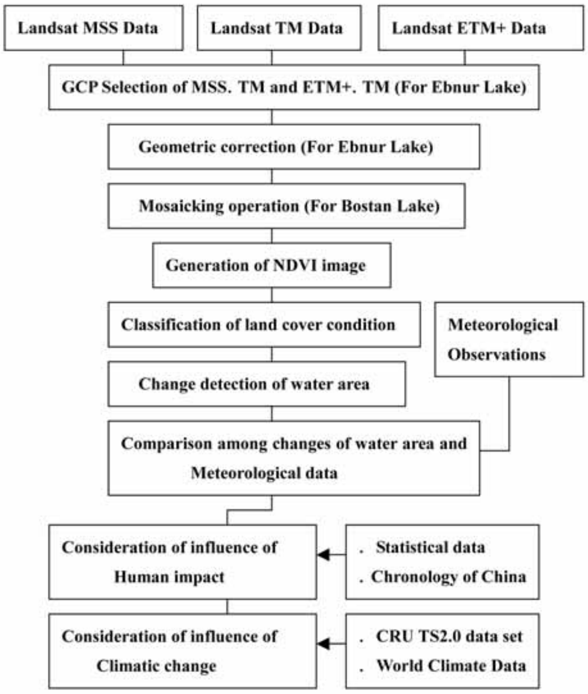

Results: Water area of lakes

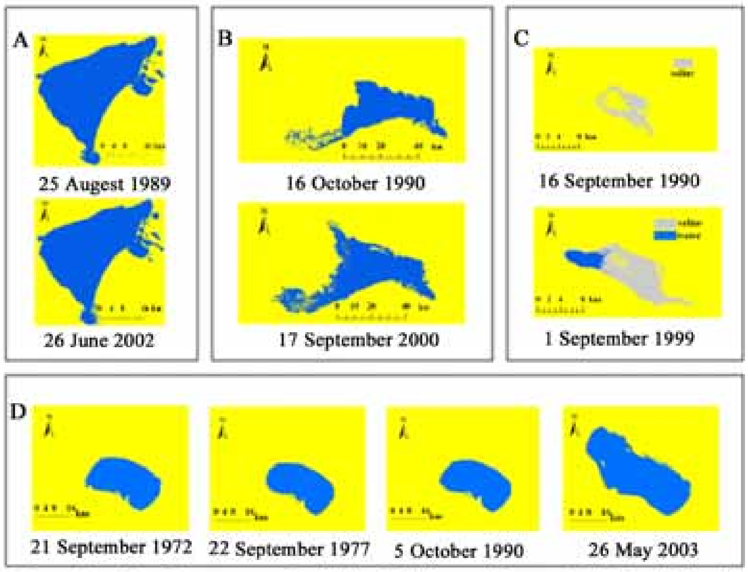

Change detection of water area of each lake(A:Wulungu,B:Bostan,C:Ayding,D:Ebnur)

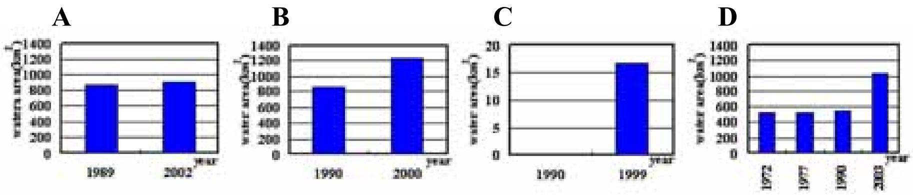

Rivers outflow

1956~1986

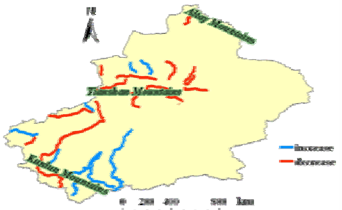

1987~2000

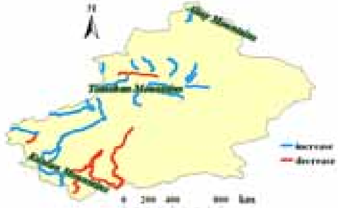

There were 65% of decreased rivers and 35% of increased rivers between the period of 1956~1986. Most of the decreasing processes were happened in north XinJiang, and most of the increasing processes were happened in south XinJiang in that period. On the contrary, there was a significant change, which has occurred during the period of 1987~2000 when the outflow of the 77% rivers have doubled, and the slight of outflow of the 23% rivers have decline. Remarkable increase was in north XinJiang and a slight decrease was in south XinJiang during this period.

Climatic factors

(1991~2000)-(1951~1990)

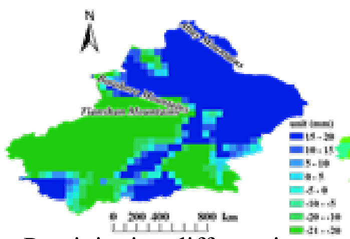

Precipitation differencing

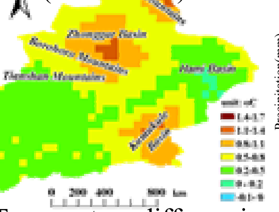

Temperature differencing

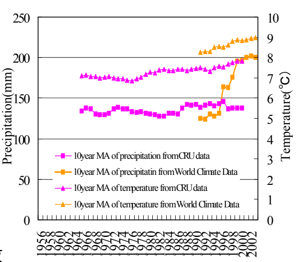

Socio-economic factors

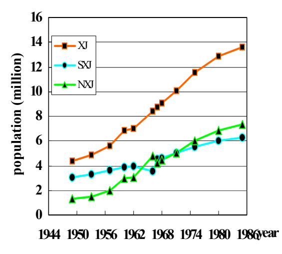

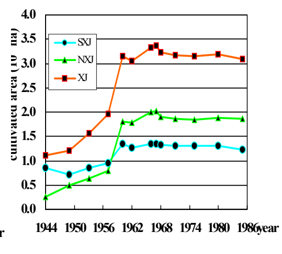

Validation of ocean color in the western equatorial Pacific Ocean by using in situ spectroradiometer and ocean color satellite data

Katsutoshi Kozai (Kobe University Faculty of Maritime Sciences)
Kensuke Tanaka (Kobe University Graduate School of Science and Technology)

In the western equatorial Pacific Ocean high sea surface temperature area is well known for the warm pool. This makes the area highly convective, which in turn influences the visible and infrared wavelength sensor signal through clouds and water vapor. In situ spectral radiometry for sea surface is inevitable for calibrating and validating physical and biological parameters such as sea surface reflectance and chlorophyll-a concentration without atmospheric corrections of remotely sensed data. The purpose of the research is to not only validate sea surface reflectance and chlorophyll-a concentration derived from MODIS but also investigate the parameters affecting sea surface reflectance by using a radiative transfer code known as 6S (version 5.2B).

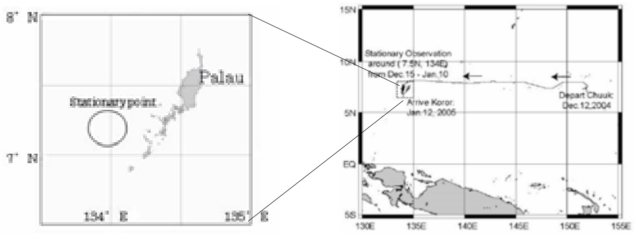

Fig.1 Study area and the stationary point (circle on the left figure, Dec.16, 2004~Jan.7, 2005).

Fig.2 R/V MIRAI and onboard spectroradiometer GER1500.

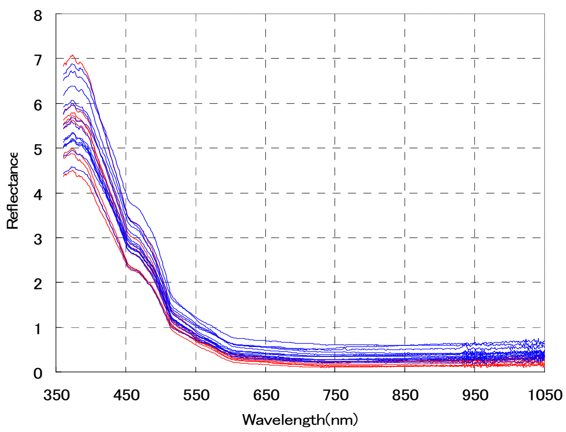

Fig.3 Spectral reflectance curves (red: before Dec.25, blue: after Dec.26, 2004)

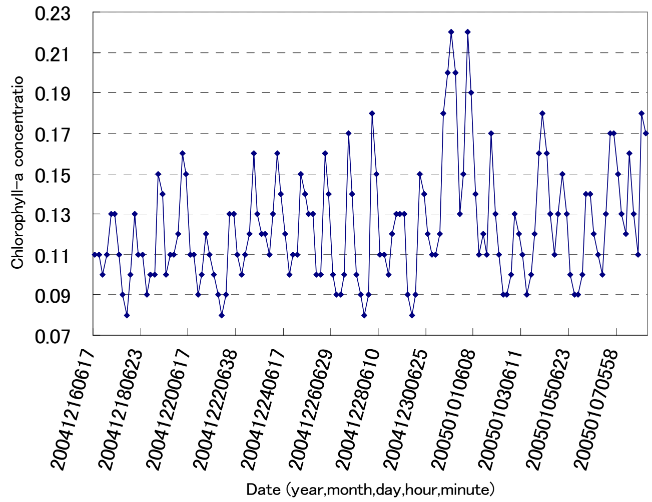

Fig.4 Variation of in situ chlorophyll-a concentration.

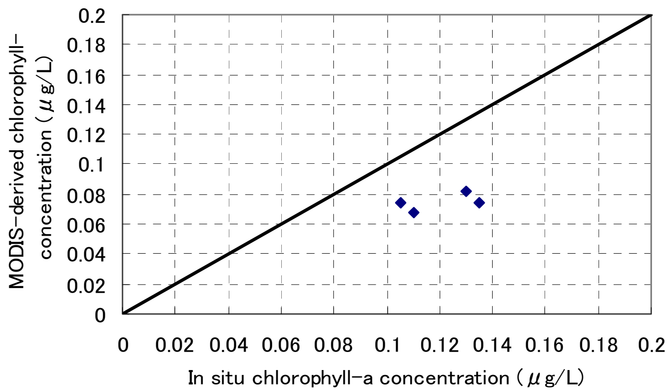

Fig.5 Comparison of MODIS-derived chlorophyll-a and in situ chlorophyll-a concentration.

Summary

(1) The maximum spectral reflectances are observed between 370~380nm and the minimum spectral reflectances are observed over 700nm.

(2) MODIS-derived chlorophyll-a concentration was underestimated comparing with in situ chlorophyll-a concentration.

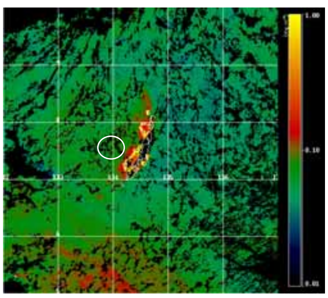

Dec.16
4h20m (UT)

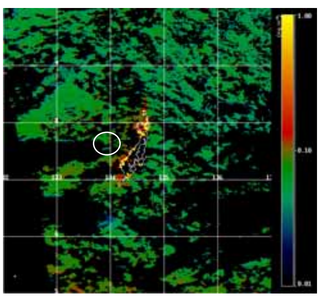

Dec.20
3h55min (UT)

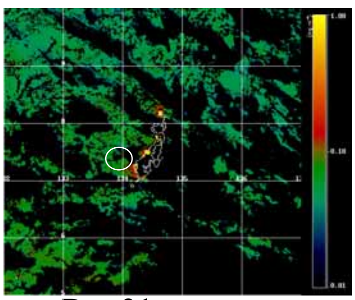

Dec.21
4h35min (UT)

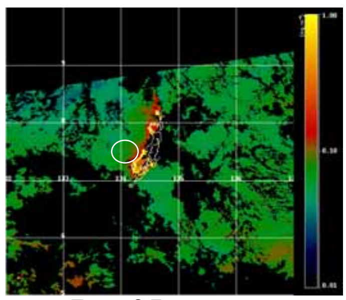

Dec.25
4h10h (UT)

Urban Change Monitoring using Former Japanese Army Maps and Remote Sensing

Chiba University

CEReS Center for Environmental Remote Sensing Chiba University Japan

J. Tetuko S.S[1]., I. Indreswari S.[2], and R. Tateishi[1]

1) Center for Environmental Remote Sensing, Chiba University

2) Department of Architecture, Institute of Technology Bandung

Institute of Technology Bandung

Abstract

In this research, urban change area of Jakarta city, Indonesia is derived by employing old maps of VOC, former Japanese Army and Indonesian Army – US Army Joint Mapping maps, and satellite imageries as KH-7/Gambit, Landsat MSS and Landsat TM. The result of this research can enrich the lack of urban area spreading of Jakarta city before 1980s. The result shows the Jakarta area (661 km^2) became urban area completely in 1990s with population about 8.5 millions.

Method

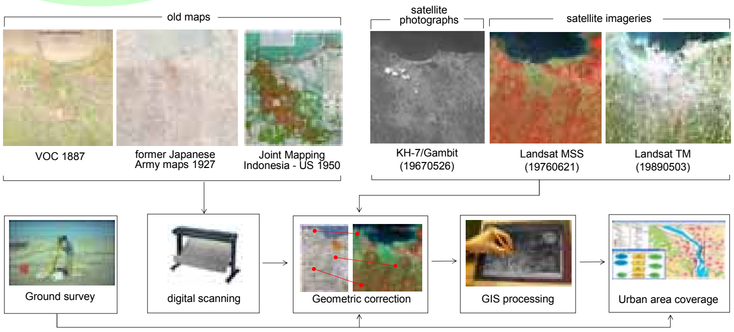

Fig. 2 Research flow-chart

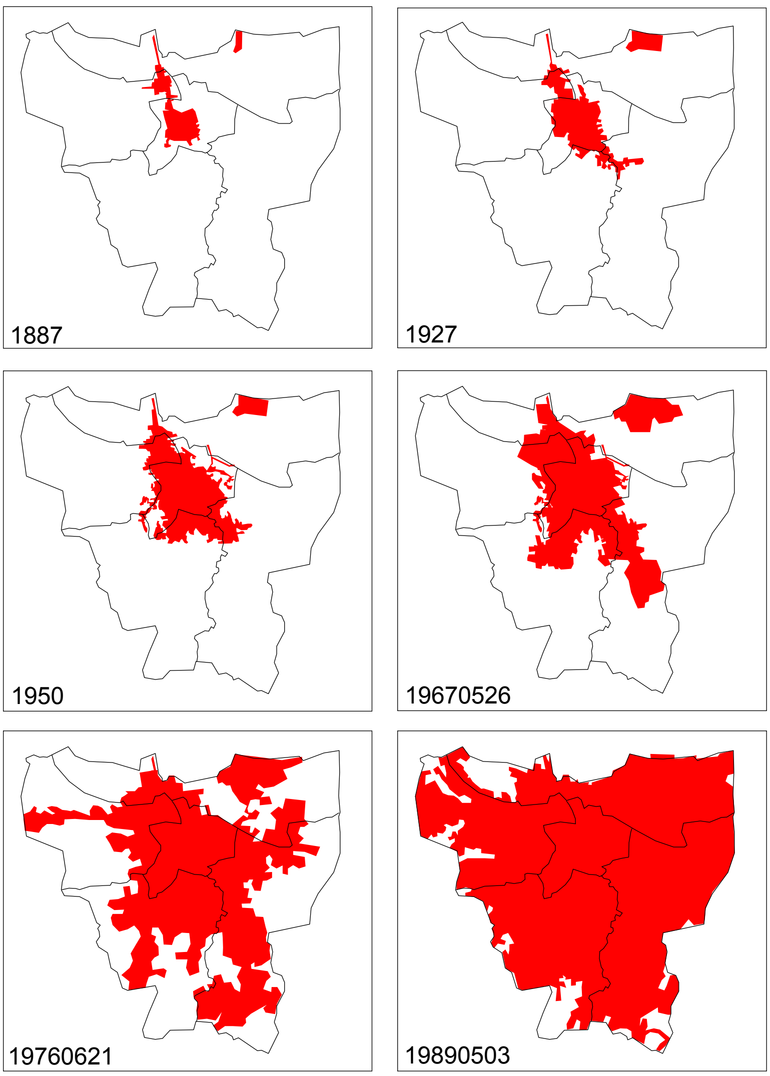

Fig. 3 Urban change of Jakarta city from 1887 to 1989

Study site

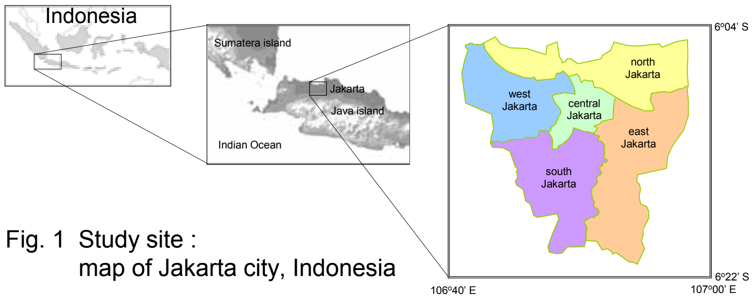

Fig. 1 Study site : map of Jakarta city, Indonesia

Sources

Maps

1. VOC 1887 [1]
2. Joint Mapping Indonesia Army – US Army 1950 [1]
3. Former Japanese Army maps 1927 [2]

Satellite images

1. KH-7 / Gambit 19670526
2. Landsat MSS 19760621 [3]
3. Landsat TM 19890503 [3]

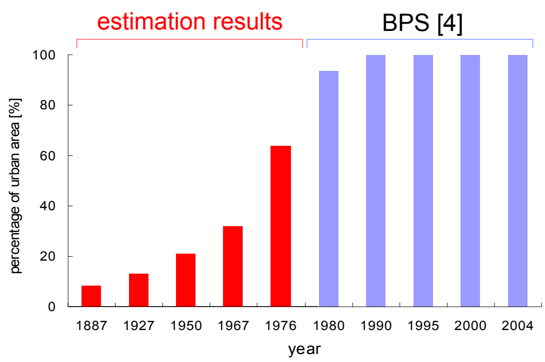

Fig. 4 Percentage of urban area versus year

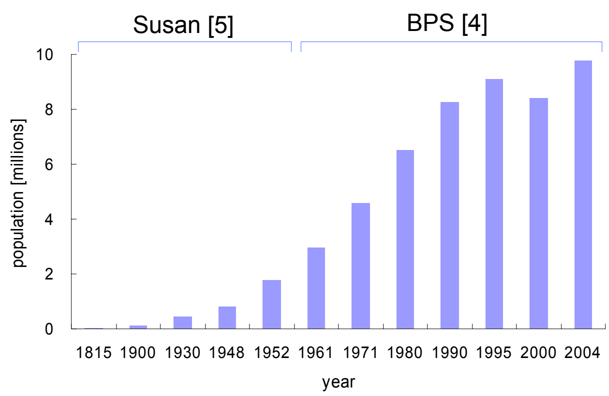

Fig. 5 Population versus year

References

1. Pandhito Panji Foundation Archive
2. Former Japanese Army maps : Possession of the Museum of Natural History, Faculty of Science, Tohoku University, Japan
3. Global Land Cover Facility, University of Maryland, United States
4. BPS : Statistics Indonesia
5. Susan Abeyasekere, Jakarta : A History, revised edition, Oxford University Press, 1990.

Cloud characterization in Chiba area from dual-site lidar observation and NOAA-AVHRR satellite

Gerry Bagtasa[1], Cheng Liu[1,2], Hiroaki Kuze[1], Nobuo Takeuchi[1], Suekazu Naito[3], Akihiro Sone[4], Hirofumi Kan[4]

1 *Center for Environmental Remote Sensing, Chiba University,* 2 *Science and Technology University of China*

3 *Chiba Prefectural Environmental Research Center,* 4 *Hamamatsu Photonics K.K.*

Abstract

Cloud heights and cloud types are characterized from the lidar data observed by two continuously operated portable automated lidar (PAL) systems and images from the visible and thermal infrared channels of NOAA16-AVHRR. The PAL systems are located in Chiba and Ichihara city areas, separated by approximately 10 km from each other. Measurements from October 2003 to March 2004 reveal that similar cloud structures are observed especially when the wind is along the path connecting the two sites. Slight time lags are frequently observed in the cloud occurrence, and they can be explained from the wind velocity data in the region. Monthly average of cloud base height (CBH) and cloud cover ratio show good correlation between the two sites. Cloud-type classification using a threshold technique in split window data of NOAA16-AVHRR gives results that are found to be consistent with the PAL cloud observations

Introduction

Cloud information such as the cloud type, structure and altitude is of importance for a variety of meteorological and climatological applications. By intercepting the solar radiation, clouds have a cooling effect on the earth's surface. Knowledge of cloud properties can give us the thermodynamic and hydrodynamic structure of the atmosphere. The height of an inversion layer can often be related to the cloud appearance.

In this study, we compare the ground-based lidar observations with the satellite-derived cloud information over the Chiba area, continuously unaided operation of PAL allowed for long term cloud monitoring without sacrificing the high temporal and spatial resolution, also, this study validates the usefulness of the split-window technique in the cloud classification.

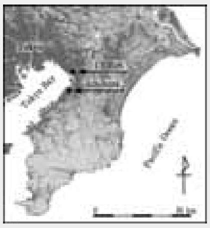

CEReS PAL

Ichihara PAL

Lidar data are obtained from two identical portable automated lidar (PAL) systems. One of the PAL systems is located in Ichihara, at the Chiba Prefectural Environmental Research Center (CERC) (35.52N, 140.07E), while the CEReS PAL system is on the main campus of Chiba University (35.62 N, 140.12 E). These two sites are about 10 km apart from each other (refer to figure above). Both are Mie scattering lidar systems capable of measuring backscattered radiation of up to 15 km in altitude. Specifications of the two PAL systems are given in Table 1. Both systems are equipped with automatic realignment systems that adjust laser beam directions every 15 min to ensure proper lidar alignment.

Table 1: Portable Automated Lidar System Specification

	Ichihara	**Chiba Univ.**
Configuration	Co-axial 38^0 slant path	Co-axial 90^0 Vertical
Laser	LD-pumped Q-switch Nd:YAG	
Wavelength	532nm	
Repetition rate	1.4 kHz	2.5 kHz
Laser energy	15mJ	
divergence	50μrad	
Receiver		
Diameter	20cm	
Type	Cassegrain	
Field of view	0.2 mrad	

Table 2: NOAA-16 Specification Orbital characteristics

Orbit inclination	98.8 deg
Mean altitude (km)	851
Equator crossing time	Northbound 13:54A Southbound 1:54D
Period (min.)	102.1
AVHRR characteristics	
resolution	1.1 km
Swath width	3000 km
Spectral range / IFoV	
Channel 1 (visible)	0.50 - 0.68 μm / 1.39mrad
Channel 4 (infrared)	10.3-11.3 μm / 1.41 mrad

The next figure shows the two-dimensional diagram whose axes are the brightness temperature of the ch.4 data and the brightness temperature difference (BTD) between the ch.4 and ch.5 data with threshold values used in the present analysis. The classes are cirrus (Ci), dense cirrus (with emissivity greater than about 0.8), cumulo-nimbus (Cb), and cumulus (Cu, including stratocumulus). The hatched area above Cu indicates non-classifiable region.

Here we have adopted slightly different threshold values (as compared to literatures) for the cloud retrieval over the Kanto plain area. This adjustment has been attained by inspecting visible, infrared, and BTD images. The result shows that (i) cirrus clouds show relatively larger values of BTD, (ii) cirrus clouds have low reflectivity and are relatively cold, (iii) cumulus clouds exhibit small BTD, and (iv) cumulus clouds have relatively high reflectivity in visible images and relatively warm in infrared images. By this method, very thin cirrus clouds can be detected, even if they cannot be seen clearly in visible images. Cumulus cloud cover is also retrieved reasonably well.

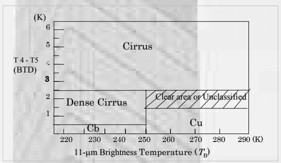

- Split-Window Measurements is based on a threshold technique in the two-dimensional histogram.
- The vertical axis is the brightness temperature difference (BTD) between the split-window data
- The horizontal axis is the brightness temperature of 11-μm channel data

Results – 5 November 2003

CEReS PAL

Ichihara PAL

- Data on 2300H of 4Nov to 0400H of 5 Nov 2003
- Clouds seen at around 2 km for both site
- data indicative of low-altitude cumulus clouds

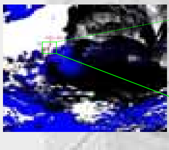

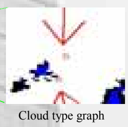

Cloud type graph

Legend
Green – dense cirrus
Yellow – cumulonimbus
Blue – cirrus
White – cumulus
Black – blank/unclassified

- Satellite data on 5 November 2003 at 0100H JST
-Mostly cirrus (blue) with patches of cumulus (white)
- Consistent with PAL data

Results – 26 August 2004

CEReS PAL

Ichihara PAL

- Data on 26 August 2004 from 0000H to 0500H
- Clouds seen at around 2 km for both site
- "shadows" formed above clouds suggesting high optical thickness
- data indicative of low-altitude cumulus clouds

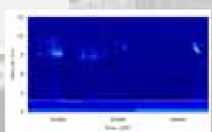

Pal data displayed with altitude up to 15 km shows geometrically thick clouds around 9 km, high altitude indicates cirrus clouds are overlying the lower cumulus clouds

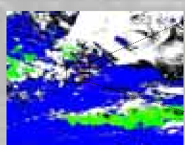

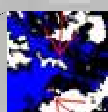

Cloud type graph

Legend
Green – dense cirrus
Yellow – cumulonimbus
Blue – cirrus
White – cumulus
Black – blank/unclassified

- Satellite data on 26 August 2004 at 0200H JST
-Mostly cirrus (blue) with patches of cumulus (white)
- Consistent with PAL data

Results - 8 March 2004

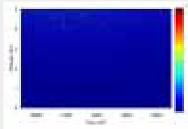

CEReS PAL

Ichihara PAL

Clear data: noon of 8 March

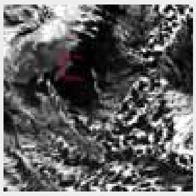

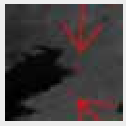

Visible channel of NOAA16-AVHRR

- Satellite data on 8 March 2004 at 1200H JST
- clear sky all throughout Chiba area
- Consistent with PAL data

Results - 3 June 2004

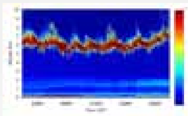

CEReS PAL

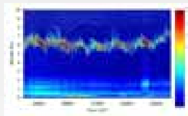

Ichihara PAL

- Data from 2300H of 2 June to 0300H of 3 June 2004
- Clouds seen at 6 to 8 km for both site
- Slant streaks indicate falling particles inside cloud (e.g. heavy ice particles)
- data indicative of mid-altitude cirrus clouds

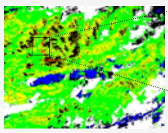

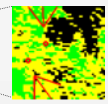

Cloud type graph

Legend
Green – dense cirrus
Yellow – cumulonimbus
Blue – cirrus
White – cumulus
Black – blank/unclassified

3 June 2004 0100H JST

- Satellite data on 3 June 2004 at 0100H JST
- Predominantly dense cirrus (green) and cumulonimbus (yellow)
- Consistent with PAL data

Conclusion

Cloud classification using NOAA16-AVHRR using split-window technique

2 PAL systems located 10 km from each other validate satellite data

Local vertical temperature profile needed for better cloud top height estimation

When satellite data has both cumulus and cirrus clouds, lidar data show only the low lying cumulus

Sandstorm mapping in Bodele depression, North Africa, with MODIS natural color images

Kithsiri Perera, Weathernews Inc, perera@wni.com
Ryutaro Tateishi, CEReS, Chiba University, tateishi@faculty.chiba-u.jp
Xia Ojy, CEReS, Chiba University, xiaojy@graduate.chiba-u.jp

Introduction

Sahara desert is the world largest Aeolian soil (fine sediments of desert sands and dust) concentration. It supplies about 50% of the Aeolian materials to oceans through sandstorms. Many studies have carried out to identify sources of these Sahara sandstorms using field investigations and remote sensing data. TOMS (Total Ozone Mapping Spectrometer) satellite data clearly detected the origin of large-scale airborne aerosols in Sahara. This figure shows a map produced by NASA using TOMS data to analyze aerosol activates (2004). This high aerosol activates are concentrated over the area from Bodele depression to the direction of Lake Chad. Recent droughts and sand storms from Bodele depression reduced Lake Chad greatly to 5% of its original size within last few decades.

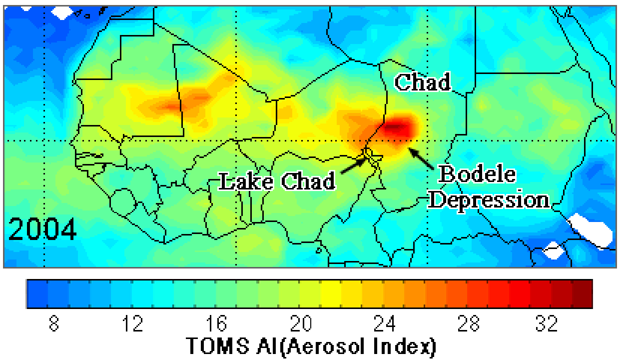

When the sandstorm is thick, nearly all signals of visible bands are returning from the top of the sandstorm to the sensor, without penetrating to the land surface. Hence, the color and tone of the image area under the sandstorm are depending on the amount of dust in the sky and the colors of underneath land cover (with the case of natural color images). Because of this, different training sites were selected from different surface colors and finally combined using wind direction information and non-sandstorm image features. Following figure illustrates the basic method used for class merging (after conducting the classification by maximum likelihood classification) in sandstorm image.

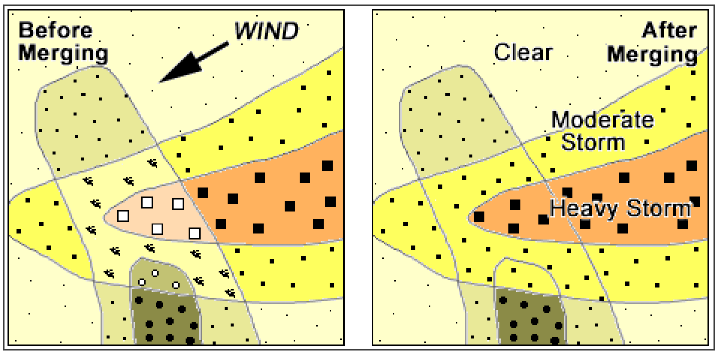

Based on above assumption, different subclasses in sandstorm-covered area were combined into three classes, in the final map as; A). **Sandstorm with 0 visibility**. B) **Sandstorm with poor visibility** (compare to non-storm image) and C). **Sandstorm with moderate visibility** (compare to non-storm image). Following 2 images are showing sandstorm and after sandstorm image.

In page 4, classified image is presented. Resulted maps gave a clear discrimination along the sandstorm thickness boundaries as well as different colors within the sandstorm. In future studies, same method can be applied to map in Bodele depression sandstorms to compare with 2005 January map (this study).

Bodele depression

Located in northern Chad, southeast to Tibesti Mountains (3415m) and Massif Ennedi highlands (1450), Bodele depression once formed a lake named Lake Megachad some thousands of years ago. The lowest point in the area is 160m. Figure shows combined MODIS mosaic of the region with elevation features. Trade winds coming from northwest are entering to the depression through the narrow passage of highlands, increasing the wind speed. These winds are uplifting find sand in Bodele depression, making this location as the most active place for sandstorms.

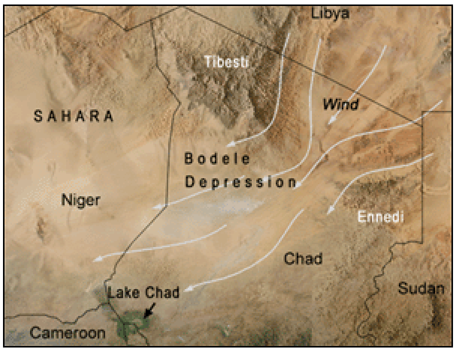

Monitoring with MODIS data

MODIS sensor data are providing an extensive amount of semi-real-time information for sandstorm observation. The approach of this study is to isolate sandstorm mass (area covered by the storm) by the conventional maximum likelihood classification method. The main advantage for this approach is the availability of sandstorm-free image data set to be used as ground truth information.

Training sites and Classification

Training sites were selected through a visual comparison of 2 images, overlaying one over the other, 2005010.aqua.250m : Sandstorm image (least visibility from the space) and 2005024.terra.250m : Non-sandstorm image. Training site identification and classification conducted by knowledge based approach, using digital data files. Study area covers about 99,000 sq km (4400 x 3600 pixel).

Bodele Depression MODIS Natural Color Image Sandstorm (Left image 050110) After the storm (050124)

Bodele Depression Sandstorm Map 050110

Original Map (250m) = 1100 x 900 km

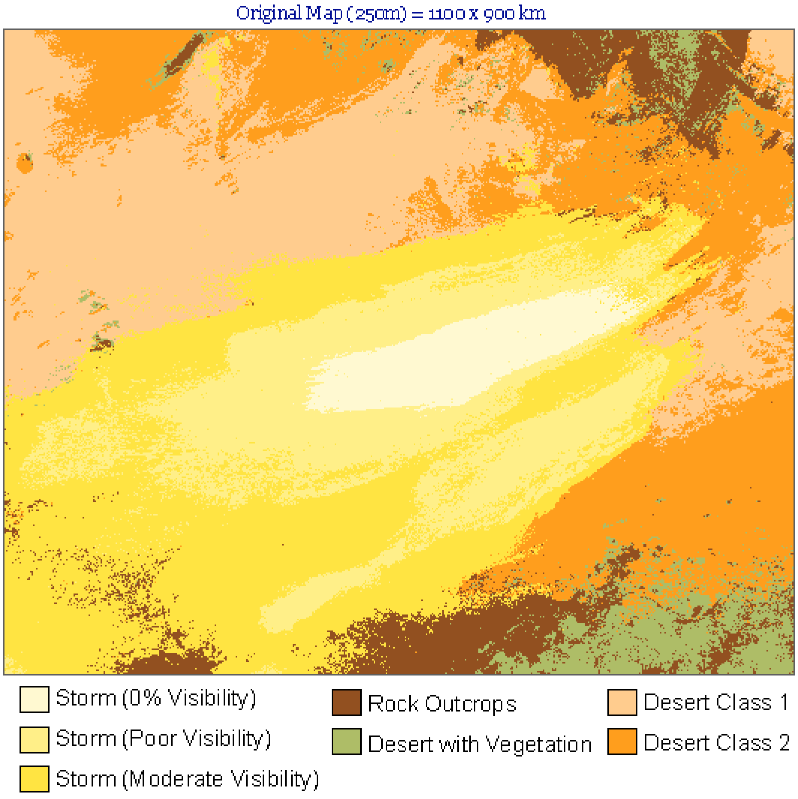

Comparison of monitoring applicability between Crop Production Index and conventional methods using satellites

By Daijiro KANEKO
Matsue National College of Technology,
Department of Civil and Environmental Engineering,
14-4, Nishiikuma-chou, Matsue, 690-8518 Japan.
E-mail: kand@ce.matsue-ct.ac.jp

1. Background

The demand for crop production will rise as a result of population growth

in China and India.

1) Rice is an excellent grain food, which supports the gigantic population in China and India.

2) The amount of rice export is small compared with the corn and the wheat.

3) Problems with the rice production could therefore have a catastrophic effect on countries that import rice and other crops.

4) Global warming makes both heavy rain and drought more likely, increasing fluctuations in the pattern of precipitation.

2. Objectives

This paper compares the applicability of the Crop Production Index CPI with conventional methods and proves the ability of the CPI to predict poor crop production using rice yield statistics, contrasting it against conventional methods such as cumulative Growing degree day GDD, integrated NDVI, and photosynthesis rate PSN.

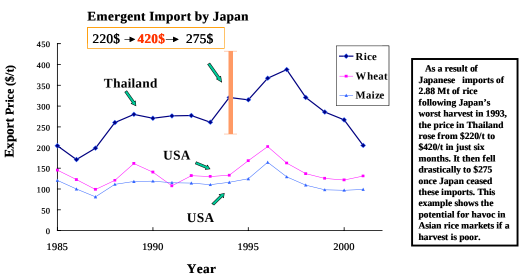

Fig. 1 Sudden rise and fall in trade price of rice compared to cheaper prices of other grains in main trading countries.

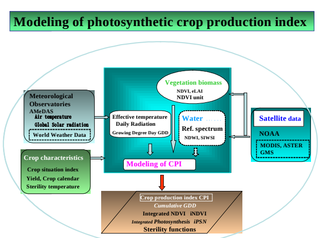

Fig. 2 Flowchart of research on crop production monitoring and development of photosynthesis type of crop production index using satellite remote sensing and world weather data.

3. Modeling

$$PSN = \frac{a \cdot APAR}{b + APAR} \cdot f_{Syn}(T_c) \cdot \beta_s \cdot eLAI \tag{4}$$

where PSN is the photosynthesis rate, $APAR$ is the absorbed photosynthetically active radiation, β_s is the stomatal opening, a and b are Michaelis-Menten constants, T_c is the canopy temperature, $eLAI$ is the effective leaf area index, and f_{ster} is the sterility response function for the air temperature.

The authors' former paper[16] presents sensitivity analysis curves for the Michaelis-Menten-type response function versus solar radiation and the temperature response of the photosynthesis rate as well known as the Sigmoidal-Logistic type function :

$$f_{Syn}(T_c) = \left[\frac{1}{1 + \exp\{k_{syn}(T_c - T_{hv})\}} \right] \tag{5}$$

where T_{hv} is the temperature parameter at half of the maximum photosynthesis rate, and k_{syn} is the slope parameter.

The temperature response functions for low-temperature sterility and high-temperature injury are defined by the following equation, referring to the curves obtained by Vong and Murata [21]:

$$F_{Lster}(T_c) = 1 - \exp[k_{Lster}(T_{Lster} - T_c)], \tag{6a}$$

$$F_{Hster}(T_c) = 1 - \exp[k_{Hster}(T_c - T_{Hster})] \tag{6b}$$

where, k_{Lster} is the low temperature sterility constant, T_{Lster} is the low sterility limit temperature, k_{Hster} is the high temperature injury constant, T_{Hster} is the high injury limit temperature, and T_c is the plant leaf temperature.

Finally, the response function of the compounded temperature sterility effects due to both low and high temperatures in grain production is expressed by the following equation:

$$F_{Ster}(T_c) = \{1 - \exp[k_{Lster}(T_{Lster} - T_c)]\} \cdot \{1 - \exp[k_{Hster}(T_c - T_{Hster})]\} \tag{6c}$$

Next, integration of the photosynthesis rate over an interval from seeding t_s to the time t of crop plant stage defines the photosynthesis-based crop production index CPI for rice having the following forms:

During crop plant stage 1, of growth:

$$CPI_U = \int_{t_s}^{t} PSN_U \cdot dt \tag{7}$$

During crop plant stage 2, of booting, heading, flowering to ripening:

$$CPI_U = F_{Ster}(T_c) \cdot \int_{t_s}^{t} PSN_U \cdot dt \tag{7a}$$

$$F_{Ster} = \int_{t_f}^{t} f_{Ster}(T_c) \cdot dt \tag{7b}$$

At the crop plant stage 3 of harvesting:

$$CPI_U = F_{Ster}(T_c) \cdot \int_{t_s}^{t_r} PSN_U \cdot dt \tag{7c}$$

$$F_{Ster} = \int_{t_f}^{tr} f_{Ster}(T_c) \cdot dt \tag{7d}$$

It is necessary to normalize the NDVI so as to remove the effect of planting area (plant coverage ratio) on the photosynthesis rate at different paddy sites. Even if the crop yield in a year was the norm, the NDVI is liable to differ each year. The plant coverage ratio per data pixel of remote sensing is dependent on the individual sites. We therefore define the standardized NDVI, called the NDVI Unit, by dividing by the annual average yield as follows:

(8)

The photosynthesis rate is similarly normalized to give the 'PSN Unit' upon dividing by the normal photosynthesis rate averaged annually, as follows:

(9)

The EPIC (Erosion-Productivity Impact Calculator) uses the same idea to normalize the effect of accumulation of Growing Degree Day, by defining the Heat Unit Index.

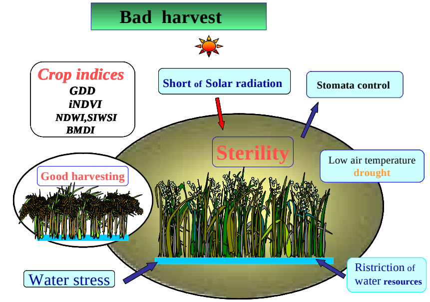

Fig. 3 Main causes of bad harvest and relating factors for monitoring rice production in the era of water resources restriction.

4. Data used in the modeling

1) Meteorological Data

The ground air temperature data, which are supplied by the Japanese Meteorological Agency from the Automated **Meteorological Data Acquisition System** (**AMeDAS**) point at ten sites, distributed in the Japanese agricultural plains, have large acreages suitable for satellite monitoring of the paddy fields.

2) Crop statistics

The Japanese Ministry of Agriculture, Forestry, and Fisheries provides grain statistical information, which includes crop situation index for the paddy rice at ten sites for monitoring and validation district. This **crop situation index** is the ratio of crop production in the year in question to the mean annual production for the ten most recent years.

3) NDVI

The satellite NDVI data used in the CPI index is the 4-minute mesh set of vegetation index data derived from NOAA Advance Very High Resolution Radiometer (**AVHRR**) by Tateishi(2001).

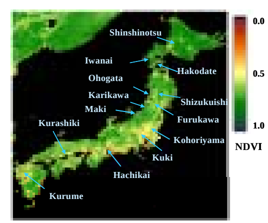

Fig. 4 Distribution of NDVI and monitoring sites in Japan for validation of Crop Production Index CPI.

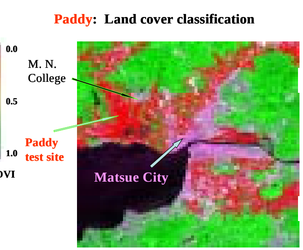

Fig. 5 Distribution of Paddy fields (red areas) in Matsue City and paddy test site.

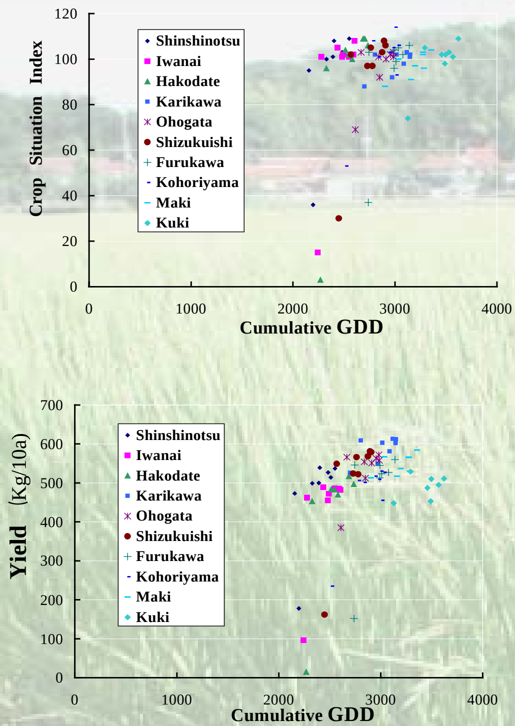

Fig.6 Comparison of monitoring applicability between Crop Production Index and conventional methods. These figures show relations between the cumulative growing degree day GDD and Crop situation index at ten monitoring points and between yield and cumulative GDD.

5. Results of crop production indices

(1) Growing index GDD

Figure 6 shows relations between the crop situation index CSI and the cumulative growing degree day (GDD), and between the yield and cumulative GDD. **The cumulative GDD** has a linear relationship to the yield but shows no ability to distinguish bad production due to low temperature sterility from normal rice yields in other years. The air temperature has two effects, on growth and ripening by photosynthesis and on pollination from heading to flowering of the grain. This sterility effect on the pollination is not linear in temperature, but cuts in rapidly below a threshold of about 18 degrees centigrade.

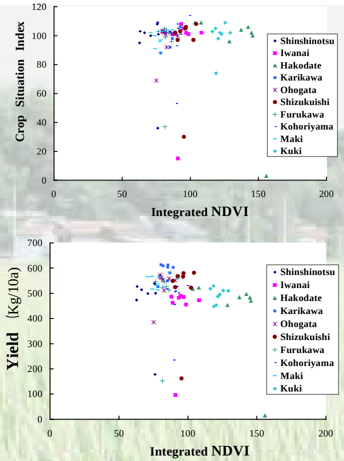

Fig.7 Relations between the integrated NDVI and Crop situation index and between yield and iNDVI.

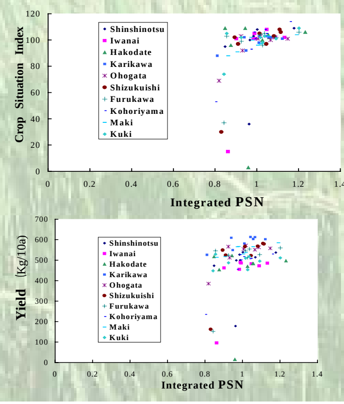

Fig.8 Monitoring applicability of integrated PSN to crop production. These figures show relations between crop situation index and integrated PSN and crop yield between iPSN.

(2) Integrated NDVI (iNDVI)

Figure 7 shows relations between the crop situation index and the integrated NDVI (iNDVI), and between yield and the iNDVI. The **integrated NDVI** is not able to predict either the crop situation index or the yield, and in particular is unable to predict a bad harvest due to low temperature sterility. The iNDVI values depend strongly on regional characteristics such as soils, type of rice and mixcel effects, involving other plants (vegetables, trees, etc.).

(3) Integrated PSN (iPSN)

Figure 8 shows the performance of the integrated photosynthesis rate iPSN used as a crop yield index. The crop situation index decreases linearly with iPSN but shows no ability to predict low temperature sterility, because sterility is not dependent on photosynthesis but is related to flowering and pollination. The **iPSN** performs much better than the iGDD or iNDVI since it is linear with respect to crop yield; however, the iPSN values show considerable scatter arising from dependence on regional conditions.

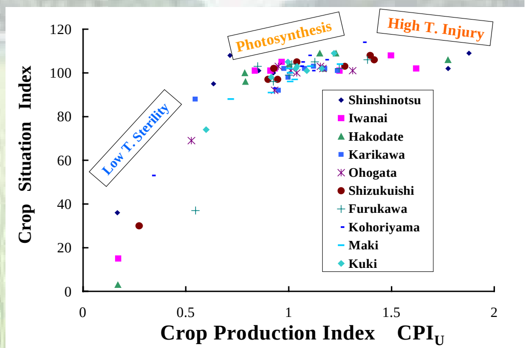

Fig. 9 Relation between the crop production index CPI_U and Crop situation index at ten monitoring points.

(4) Photosynthesis type of crop production index CPI

Figure 9 shows the relation between crop situation index CSI and the CPI_U, to verify applicability to rice yields at 10 sites in Japan. Abnormal weather with low temperature and much cloud causes low temperature sterility and late ripening of rice. The **CPI_U** then rapidly falls to zero, since the limiting problem is not photosynthesis but inadequate flowering and late ripening in the worst case of the crop situation index below 50 in 1993.

6. Conclusions

1. Consequently, only CPI_u is able to predict a bad harvest due to sterility effects, by making the CPI_u values decrease sharply to zero based on the eigen-functional relationship between CPI_u and the crop situation index CSI, as well as the yield.
2. The validation exercise clearly proves the **superior** ability of the present index to predict poor production using rice yield statistics in comparison to conventional methods such as cumulated growing degree day GDD, integrated NDVI, and photosynthesis rate PSN.
3. The method is based on routine observation data, allowing automated monitoring of crop production at arbitrary sites without any special observations.

Geologic Information Retrieving using Synthetic Aperture Radar

Chiba University

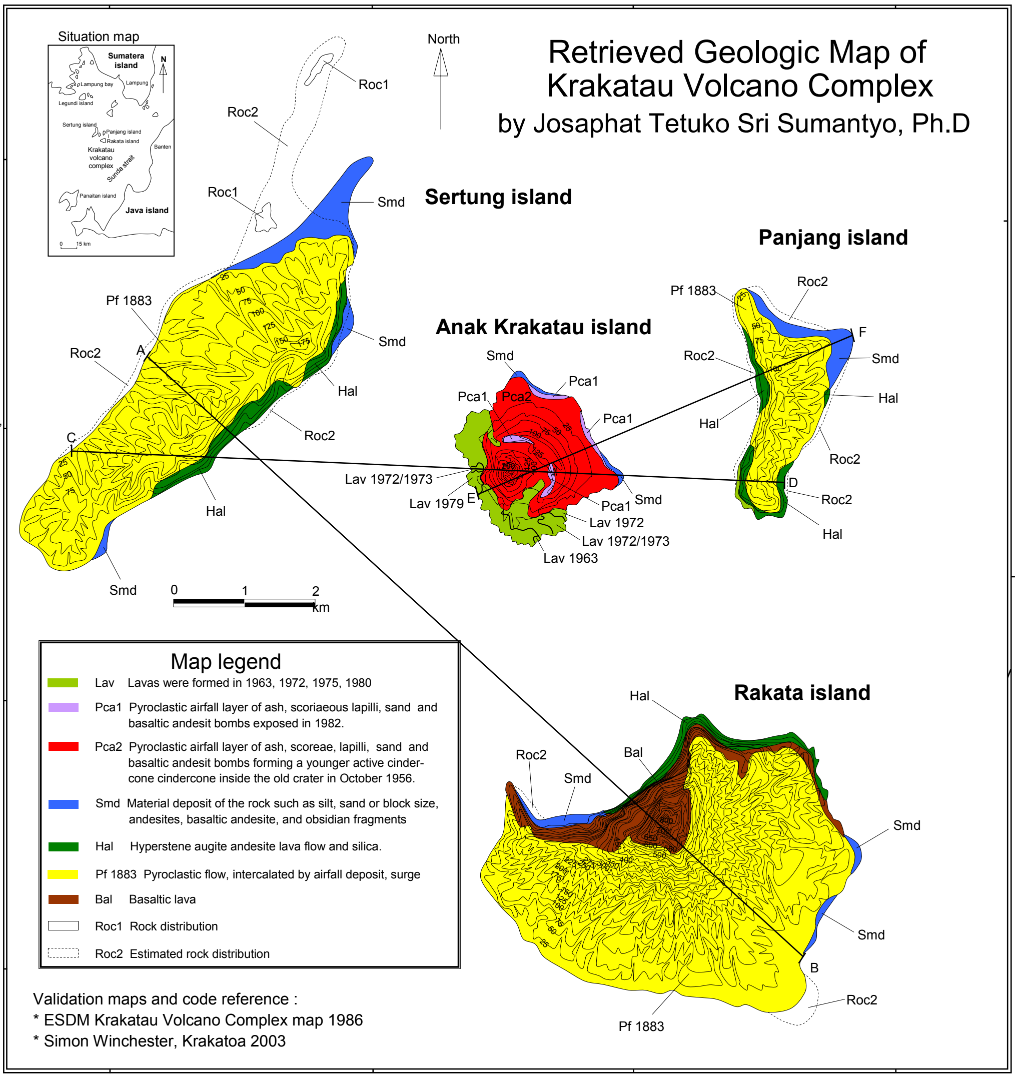

The birth of Krakatau volcano complex

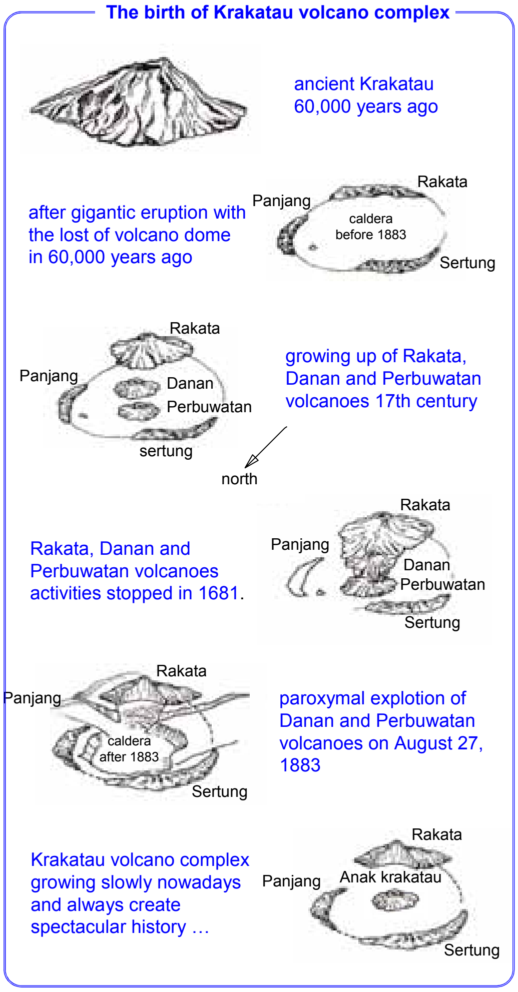

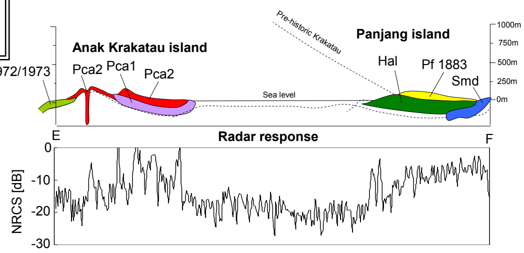

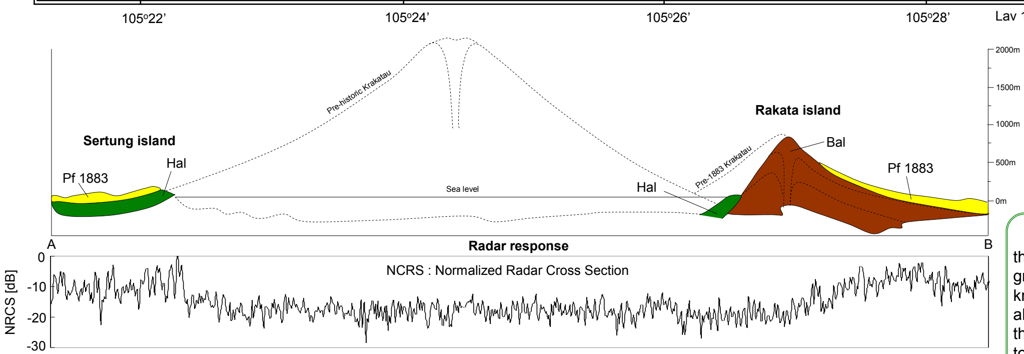

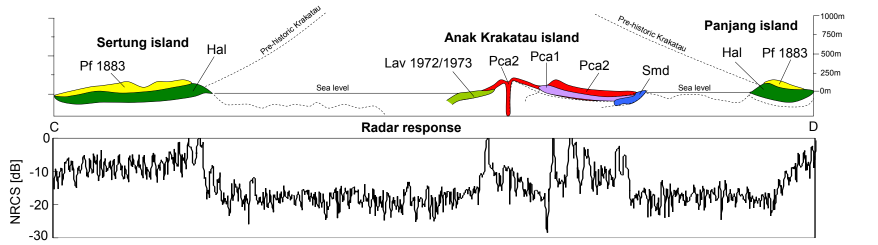

Historic eruptions and recent activities

Krakatau was well known and became famous in the world because of the paroxymal eruption on August 27, 1883 and it was considered to a great event of the eruptive history, which has erupted more than 18 cubic km of ash column of about 80 km high, and rose tsunami as high as 30 m along the west coast of Banten and south coast of Lampung. Although at that times the big cities have not developed as such today, but 295 small towns were swept by tsunami and killed 36, 417 people (Verbeek,1884), and the explosion could be heard at Africa, Australia, Philippine etc or 4800 km far away. Krakatau began to be known in the eruptive history when the gigantic eruption occurred in 416 BC, which caused a tsunami and formed a caldera (Judd, 1889). Furthermore De Neve (1981) noted some information that before the second paroxymal eruption 1883, several large eruptions of Krakatau arose in the centuries of 3,9,10,11,12,14,16 and 17 which were followed by growing up of Rakata, Danan and Perbuwatan volcanoes. This volcanic activity stopped in 1681. After reposing of about 200 years, Krakatau began to indicate its activity which has preceded by the eruptions of Danan and Perbuwatan volcanoes. On May 20, 1883 the eruption of Perbuwatan volcano with basaltic composition, initiated a paroxymal explosion on August 27, 1883 (Neumann, 1951).

Second repose period of Krakatau began in February 1884 to December 1927, when the first phase of eruption on December 29,1927 occurred as a submarine explosions in the center of Krakatau Volcanic Complex. The visible phenomena of the eruption comprised bublings and fountains of seawater (Stehn, 1929a). It was observed on January 20, 1929 the crater-rim appeared east of the eruption point, consisting of ashes, lapilli, loose block. It formed an island above the water and was named "Anak Krakatau" (Child of Krakatau). The eruptions continued until February 15, 1929 where the explosion column reached a height of 800 m. Observations on February 18, indicated that the eruption was no longer visible and the Anak Krakatau island was shaped like a sickle, opening to the south west, and which had reached a height of 38 m above sea level. This event was declared by Stehn as a birthday of Anak Krakatau.

(Article source: Directorate of Volcanology and Geological Hazard Mitigation, ESDM, Indonesia and Krakatoa by Simon Winchester)

Contact person :
Josaphat Tetuko Sri Sumantyo, Ph.D
Center for Environmental Remote Sensing, Chiba University
1-33, Yayoi, Inage, Chiba 263-8522 Japan
Tel. +81 (0)43 290 3840 Fax +81 (0)43 290 3857
Email jtetukoss@faculty.chiba-u.jp
http://www2.cr.chiba-u.jp/lab/jtetukoss/

Satellite Observation and Analysis of Terrestrial Environmental Changes

Development and Publication of Land Cover and Vegetation Datasets at Regional and Global Scales

H. Sasaki[a], H. Nakajima[a], T. Okatani[a], Y.Numata[a], Y. Yamada[a] and R. Tateishi[b]
a: Geographical Survey Institute, b: Chiba University

Summary: With the participation of 155 National Mapping Organizations of all over the world, ISCGM (International Steering Committee for Global Mapping), whose secretariat is hosted by Geographical Survey Institute of Japan, has been developing "Global Map." Global Map is global digital geographic framework datafor sustainable development which describes global environmental status and its changes.

ISCGM places a special emphasis on raster formatted global land cover data and percent tree cover data development, in the second phase of Global Mapping to be completed by 2007. As one of central activities of ISCGM, this joint study aims to explore effective acquisition methodology of these raster data by fully utilizing satellite remote sensing technology. Followings are the outline of Global Map and expected outcomes of this study.

What is Global Map ?

- **Digital geographic information in 1 km resolution (at app. 1: 1 million scale)**
- **To cover the whole land of the globe in consistent specifications under international cooperation**
- **Includes 8 data layers**

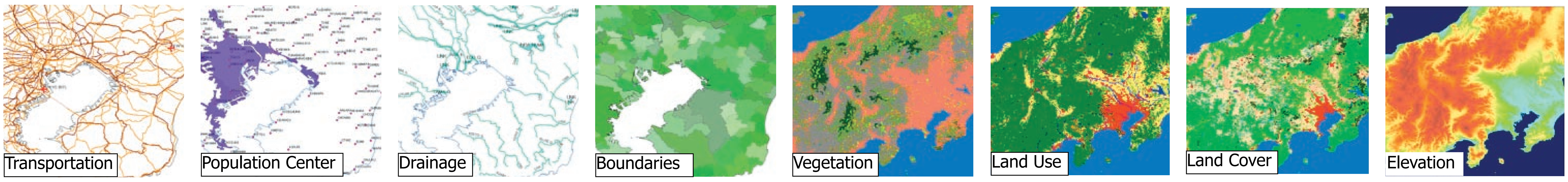

Status of Global Mapping Project

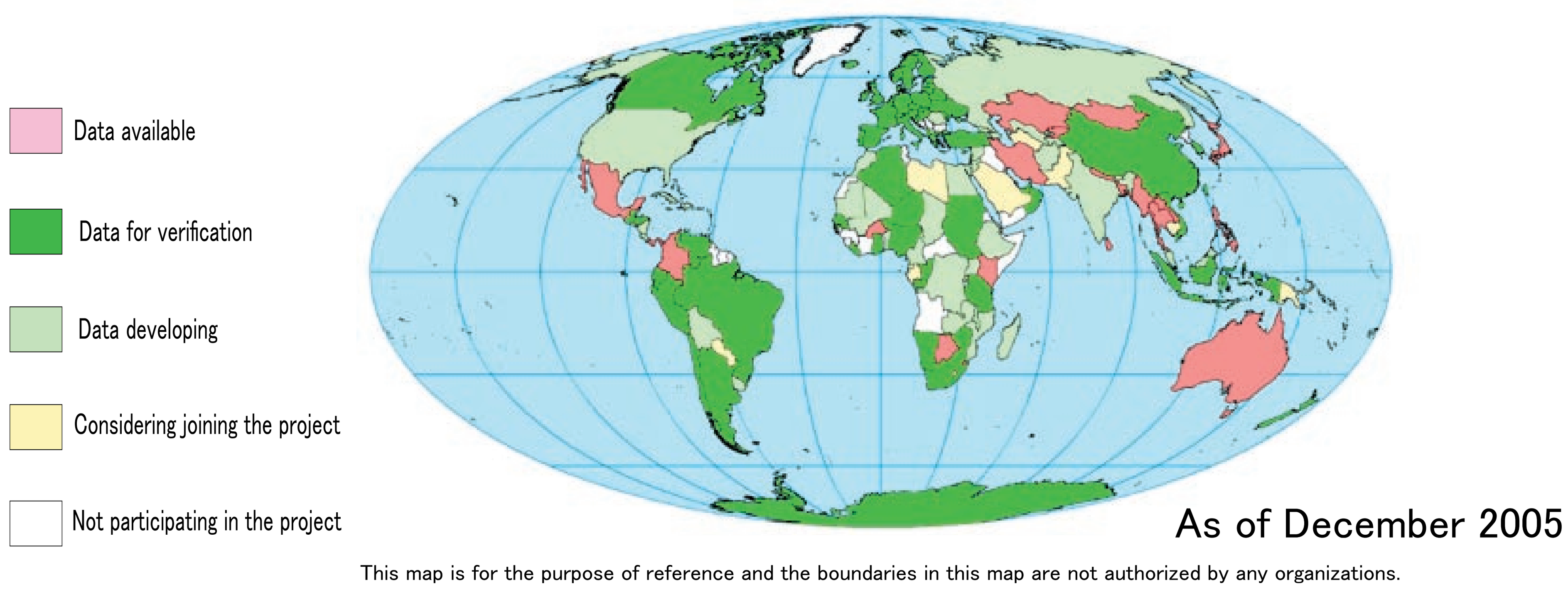

155 countries/areas participating

21 countries released Global map data

Australia	Japan	Mongolia	Sri Lanka
Bangladesh	Kazakhstan	Myanmar	Swaziland
Botswana	Kenya	Nepal	Thailand
Burkina Faso	Kyrgyzstan	Panama	
Colombia	Lao P. D. R.	Philippines	
Iran	Mexico	Samoa	

Expected Outcomes of This Study

Tree Canopy Cover